Comparative study of small-scale flat-plate direct contact membrane distillation and vacuum membrane distillation modules with integrated direct solar heating

Qiuming Ma, Aras Ahmadi, Corinne Cabassud

Comparative Study of Small-Scale Flat-Plate Direct Contact Membrane Distillation and Vacuum Membrane Distillation Modules with Integrated Direct Solar Heating

Qiuming Ma[a,b], Aras Ahmadi[b], Corinne Cabassud[b,*]

[a] Institute of Refrigeration and Cryogenics, Engineering Research Center of Solar Power and Refrigeration (MOE China), Shanghai Jiao Tong University, 800 Dongchuan Road, Shanghai, 200240, China

[b] TBI, Université de Toulouse, CNRS, INRAE, INSA, Toulouse, France

[*] Corresponding author:
Corinne Cabassud
INSA Toulouse, TBI
135 Avenue de Rangueil
F-31077 CEDEX 4, Toulouse, France
Tel.: +33 5 61559782 E-mail: corinne.cabassud@insa-toulouse.fr

Abstract

An intensified desalination module directly integrating membrane distillation (MD) and solar flat-plate collector (FPC) into the same small equipment is explicitly modeled and studied in the present article. Based on a previous work applying vacuum MD (VMD) to the integrated module and the corresponding recycling system, direct contact MD (DCMD) is also adopted in similar configurations to comparatively study the dynamic performance, the impact of different parameters, and the potential production of both DCMD-FPC and VMD-FPC modules.

Abbreviations: AGMD, air gap membrane distillation; BDF, backward differentiation formula; CP, circulation pump; CPC, compound parabolic collector; CR, concentration ratio; DCMD, direct contact membrane distillation; ETC, evacuated tube collector; FPC, flat-plate collector; HRR, heat recovery ratio; MD, membrane distillation; MED, multi-effect distillation; MSF, multi-stage flash; OAT, one at a time; PP, polypropylene; PTFE, polytetrafluoroethylene; PV, photovoltaic; PVDF, polyvinylidene fluoride; RO, reverse osmosis; SC, solar collector; SCOW, simplified cost of water; SEC, specific energy consumption; SEEC, specific electric energy consumption; SGMD, sweeping gas membrane distillation; STEC, specific thermal energy consumption; TPC, temperature polarization coefficient; VMD, vacuum membrane distillation; VP, vacuum pump.

Simulation results for a 0.35 m^2 module and a 12-hour operation show diametrically opposite performances in terms of water production and electricity consumption of these two desalination devices. Analyses on the influences of parameters indicate that the productions of both systems are limited by the incoming solar energy, and the DCMD-FPC system further suffers from conductive heat loss across the membrane. In order to relieve the performance from the restriction of available thermal energy, two approaches by heat recovery and solar concentration are applied to both DCMD-FPC and VMD-FPC to examine the potential enhancement. The results on both approaches all recommend the choice of VMD-FPC for small-scale applications, based on its more relevant productivity and less space footprint.

Keywords

Membrane distillation; direct solar heating; integrated module design; performance comparison

Nomenclature

Al	local altitude (km)
B	membrane permeability (s m^{-1})
C	salt concentration (g L^{-1}) / cost (€)
c_p	specific heat at constant pressure (J kg^{-1} °C^{-1})
D	distillate productivity (L m^{-2}) / diffusion coefficient (m^2 s^{-1})
d	diameter (m)
F	flow rate (m^3 s^{-1})
f	friction factor
G	solar radiation intensity (W m^{-2})
h	convective heat transfer coefficient (W m^{-2} °C^{-1})
i	discount rate
J	permeate flux (L m^{-2} h^{-1})
K	extinction coefficient (m^{-1})
k	thermal conductivity (W m^{-1} °C^{-1})
L	module length (m)
L_{loc}	local longitude in degrees west (°)
M	molar mass (kg mol^{-1})

m	mass (kg)
$\dot{m}$	mass flow rate (kg h^{-1})
Nu	Nusselt number
n	refractive index
Q	energy flux (W m^{-2})
P	pressure (Pa)
$\dot{P}$	power consumption (W)
Pr	Prandtl number
R	gas constant (8.3145 J mol^{-1} K^{-1})
Re	Reynolds number
r	pore radius (m) / nominal escalation rate
Sc	Schmidt number
Sh	Sherwood number
T	temperature (°C)
U	heat loss coefficient (W m^{-2} $°C^{-1}$)
V	volume (m^3)
v	flow velocity (m s^{-1})
W	module width (m)
x	molar fraction
ΔH_v	latent heat of water evaporation (J kg^{-1})

Greek letters

α	solar absorptance
β	slope (°)
γ	azimuth angle (°) / activity coefficient
δ	thickness (m)
ε	porosity / emittance
η	efficiency
θ	incidence angle (°)
λ	mass transfer coefficient (m s^{-1})
μ	dynamic viscosity (Pa s)

ρ	density (kg m^{-3})
τ	tortuosity
φ	local latitude (°)

Footnotes

a	air / ambient
ap	absorber-plate
atm	atmosphere
bo	bottom
c	cooling / cover
cp	circulation pump
D	diffusion
d	diffused / distillate
f	feed
g	gas
h	hydraulic
K	Knudsen
m	membrane
n	in normal direction
p	permeate / polymer
S	absorbed
s	seawater supply
T	total
u	utilized
V	viscous / volumetric
v	vapor
vp	vacuum pump
w	water
wi	wind

1. Introduction

1.1 Membrane distillation

In the domain of desalination, two technology categories are currently prevailing, i.e. thermal distillation and membrane separation [1]. Multi-stage flash (MSF) and multi-effect distillation (MED) are the most common applications of the former, while reverse osmosis (RO) is the dominating technology of the latter. As an emerging alternative, membrane distillation (MD) is a process based on water evaporation provoked by a difference in partial pressure between the two sides of a hydrophobic microporous membrane, which is used as the support for the liquid/vapor interface [2]. Possessing characteristics of both thermal distillation and membrane separation, MD has gained its popularity in desalination and research interest is continuously growing [3]. As a distillation process, pure distillate is obtained as the permeate and thus nearly a 100% rejection of salt and other non-volatiles is expected without pressurizing the operation as in RO [4]. Besides, much higher water recovery rate, even close to the saturation of salt concentration is achievable compared to RO because of no limitation of osmotic pressure [5]. On the other hand, the use of membrane ensures: i) a substantial interfacial area for small and compact modules and process intensification; ii) a working temperature lower than the boiling point; separation of the liquid and vapor phases. Therefore, MD is considered as a promising solution for small-scale and easy-to-operate desalination applications [6].

Generally, four different MD configurations have been widely studied in the literature, i.e. direct contact MD (DCMD), vacuum MD (VMD), air gap MD (AGMD) and sweeping gas MD (SGMD), defined by the vapor receiving structure on the permeate side [7]. Among them, DCMD is the simplest for a lab-scale MD device and thus the most studied configuration [8], where the circulating cold condensation liquid is in contact with the membrane and directly receives transmembrane vapor flux. As the second most studied configuration in the literature [8], VMD applies a vacuum environment on the permeate side to induce a difference in vapor pressure across the membrane, and consequently, an external condensation is needed to collect the permeate vapor as the distillate. Potentially, VMD represents the diametrical opposite of DCMD from the point of view of water production and electricity consumption. A higher permeate flux in VMD is expected due to the attenuated temperature polarization and transmembrane thermal loss when vacuum is exerted on the permeate side, while the addition of a vacuum pump and an external condenser in VMD elevates the electrical demand during operations.

1.2 Small-scale solar powered DCMD and VMD

In spite of all the aforementioned merits of MD processes, the heat demand is still considerable because of the latent heat for water evaporation (~ 667 kWh m^{-3} [9]). This issue becomes especially tricky when a small-scale, distributed and autonomous desalination system is desired for the applications in some remote coastal areas or isolated islands. Fortunately, the relatively low working temperature of MD (below 80°C [10]) enables the possibility of applying low-grade renewable heat sources. Indeed, the research on coupling MD with solar energy has flourished since the first practice by Hogan et al. in 1991 [11], where a hollow fiber DCMD module with a total membrane area of 1.8 m^2 was fed by the seawater heated by a solar flat-plate collector (FPC) field of 3 m^2. Simulation results indicated an impressive daily production of 50 L with external heat exchange for heat recovery. In another theoretical study on evacuated tube collector (ETC) powered flat-sheet DCMD modules [12], the authors pointed out that the efficient use of the available solar energy, which is limited by the area of solar collector (SC), is essential to system productivity, and that an adapted heat recovery strategy is the only way to enhance overall performance. In order to experimentally demonstrate a solar-driven DCMD system, a DCMD module of 3.39 m^2 was connected to a 20 m^2 FPC field and a photovoltaic panel with a peak power of 1.48 kW [13]. The system configuration with heat recovery (by heat exchanging between the permeate stream and the feed outside the module) exhibited an enhanced daily average flux of 4.59 L h^{-1} and a reduced specific energy consumption (SEC) of 1609 kWh m^{-3}, compared to the daily average flux of 3.31 L h^{-1} and the SEC of 2342 kWh m^{-3} for the system without heat recovery. Later, a numerical study on a simple FPC-driven DCMD system without heat recovery resulted in a daily freshwater production rate of 19.7 kg per m^2 of membrane or 6.3 kg per m^2 of FPCs [14]; while an experimental study on ETC-driven DCMD system with enhanced permeate side cooling showed a daily production of 26.76 - 33.55 L for a SC field of 2.61 m^2 with 1 m^2 membrane, attaining a maximum overall thermal efficiency of 49% [15]. Recently, a compact DCMD module with condensation heat recovery by heat exchange between the cold feed and the relatively warm permeate flow. Three FPC, each 2 m^2, and a photovoltaic (PV) panel of 1.63 m^2 were installed to furnish the DCMD system with thermal and electric energy. The test results showed that 86 L of freshwater could be daily produced in Kairouan, Tunisia.

On the other hand, studies on small-scale solar-driven VMD systems have been less witnessed. A tiny hollow fiber VMD module of 0.09 m^2 powered by 8 m^2 SCs was built and experimentally tested [16], and a daily total production of 173.5 L was obtained at a fairly high cost: a specific thermal energy consumption (STEC) of 7858 kWh m^{-3} and a specific electrical energy consumption (SEEC) of 317 kWh m^{-3}, probably because of the uncoordinated surface areas of the membrane and the SCs. Later, an ETC of 2.16 m^2 was applied to provide heat for a 0.25 m^2 flat-sheet VMD module [17], yielding an average permeate flux of 4 L m^{-2} h^{-1} (in terms of membrane area) and an STEC of 750 kWh m^{-3}. Applying both ETC and PV panels to power a VMD system [18], an SEEC of around 80 kWh m^{-3} was reported. The adopted surface areas of ETC, PV system and membrane were 1.82 m^2, 1.62 m^2 and 0.1 m^2, respectively. In the experiment, the excess electricity generated by the relatively large PV system was used to heat the feed storage tank, aiming to fully capitalize the captured solar energy.

In order to more efficiently consume the collected solar energy for distillation and to further shrink the module size for domestic applications, efforts on directly integrating SC and MD have been intensively witnessed since the 2010s, which can avoid the heat and pressure loss in piping and connections, intensifying the whole desalination process [19]. In 2009, a solar distillation device containing a flat-sheet AGMD module was built and studied [20], being the first practice of this integrated SC-MD configuration, but the exhibited daily production was only 2.18 L m^{-2} day^{-1} at an SEC of 2880 kWh m^{-3}. Later, this idea was applied to DCMD and VMD modules. In the experimental and modeling work by Chen and Ho [21], the feed side of a DCMD module was placed in the space under the absorber-plate of an FPC, where the feed circulation was directly heated by the absorbed solar energy. However, the integrated module was not dynamically studied as an independent solar desalination system, and no daily accumulated production was provided by the authors. Additionally, other MD configurations, such as VMD, were not included as a comparison.

For VMD, an indicative study on different solar-driven flat-sheet VMD module concluded that the integrated VMD-SC module would yield better performance [22]. Later, a direct integration of FPC and VMD by Ma et al. [6] in the same module was extensively studied and dynamically modeled to illustrate the technical feasibility and the performance at small-scale in compact systems, for instance for production of drinking water in remote coastal areas or isolated islands with no heat provision. Dynamic simulation results revealed a daily production of 8 L m^{-2} at an SEEC of more than 200 kWh m^{-3}, along with a much higher potential and system performance if considering a feasible heat recovery strategy from condensation. For instance, for a heat recovery ratio of 0.5, up to 15 L m^{-2} of water could be produced with a specific pumping energy consumption lower than 121 kWh m^{-3}.

Hollow fiber VMD modules were also applied to integrated devices. The numerical study on inserting hollow fiber membranes into the cylindrical absorber of a compound parabolic collector (CPC) provided an innovative approach to intensify the sparse incoming solar energy for VMD process [23]. Later, an integrated hollow fiber VMD desalination device was fabricated and experimentally studied [24]. The tubes of an ETC with a total aperture area of 1.6 m^2 were filled by hollow fiber membranes of 0.2 m^2, and the test results showed a daily freshwater production of 3.2 ~ 4.8 L at a calculated STEC of more than 1000 kWh m^{-3} and an SEEC of 208 ~ 313 kWh m^{-3}, which is in the same range as the previous work on flat-sheet VMD-FPC [6]. A similar configuration was employed to integrate VMD with ETC [25], applying natural convection flow mode without adding circulation pumps. The daily water production reached 6.7 L per m^2 of the solar collector at a thermal efficiency of 51%, exceeding the previous study. The same configuration was also tested for DCMD earlier by the same research group [26], and the results showed a lower production rate than VMD, being merely 0.37 L h^{-1} per m^2 of the solar collector. Additionally, they claimed a 17% increase in DCMD performance compared with the configuration where DCMD module and ETC were separately installed. The comparison between the same integrated configuration respectively using VMD and DCMD is yet to be reported.

1.3 Research objective

The limitation by the available solar energy and the factor of heat recovery have already been proven essential in the reported studies on solar-driven MD systems where SC and MD modules were separated, as described in Section 1.2. Even though the process is more intensified and the loss in connections is exempted in the above-reviewed integrated MD-SC modules, the potential production with the help of heat recovery or other approaches enhancing the incoming thermal energy for MD has rarely been discussed.

On the other hand, comparisons made in the literature between DCMD and VMD [27–32] have already pointed out that VMD is advantageous in terms of the permeate flux and thermal energy efficiency due to the negligible conductive heat loss, while DCMD is simpler in system layout and operation. However, most of these comparisons were only qualitative, and even the quantitative studies were mostly based on fixed feed conditions, especially fixed feed temperature levels, which is not the case in any independent solar powered MD system [33]. Moreover, the evaluation of energy consumption in the above-mentioned comparisons was either totally absent [28–30], or provided partially without considering the intensive cooling demand for permeate vapor condensation under the vacuum in a conventional VMD [27,31,32].

Hence, it becomes interesting to quantitatively compare the VMD-FPC system with a similar configuration (MD-SC) using the well-known DCMD, considering different working conditions and performance enhancing measures. Besides, particular measures, such as draining or auxiliary heating, have to be taken when the ambient is freezing cold, because such an MD-SC configuration can only work at a temperature above ice-point. But these measures are out of the scope of the current study. In the present work, the comparative study between VMD-FPC and DCMD-FPC is performed through simulations for the same size and the same concept of the flat sheet integrated module. Therefore, evaluations are presented to observe and compare the energy consumption and the production of the two systems, when considered at a global scale accounting required energy inputs. In addition, detailed analyses on the impact of different parameters are carried out to identify the main factors contributing to the improvement of both systems. Finally, discussions on their different hybridization perspectives by applying heat recovery strategy or solar concentration factor within a solar-MD desalination module are presented to recommend a better choice between these two.

2. Module & system description and modeling

Cooling for the distillate recirculation has to be configured in the case of DCMD-solar desalination module, in order to maintain the temperature difference between the feed and the permeate side. In this regard, a constant flow of cold seawater source is usually placed in direct heat exchange with the permeate side of DCMD. To provide a fair comparison, a very close system description has been applied here for VMD-FPC and DCMD-FPC. However, certain necessary readjustments for DCMD-FPC system based on the previous VMD-FPC system [6] have been additionally involved: (i) a slight change of module configuration in DCMD-based module should be made, as later described in Section 2.1, which implies that the permeate side of the DCMD-FPC module becomes the cold circulating distillate; (ii) the diffusion mechanism inside the membrane pores for DCMD and VMD is not the same because of the difference in pore pressure, a different description of membrane permeability has to be adapted for DCMD and will be further described in Section 2.2, instead of a using the coefficient for Knudsen diffusion as proposed for VMD [6]; (iii) the recirculation of the cold distillate on the permeate side has to be considered and added to system dynamics, together with a simple cooling cycle for the permeate side to keep the transmembrane vapor pressure difference. Detailed descriptions and system dynamics in this regard will also be provided in Section 2.3.

2.1. DCMD module configuration

The configuration of the considered DCMD-FPC module is shown in Figure 1. Solar radiation passes through the glass cover and get absorbed by the absorber-plate of an FPC, heating the DCMD feed side by direct contact. The feed side and permeate side are both beneath the absorber-plate, separated by the membrane with saline water and distillate water circulating counter-currently. A temperature difference is created between these two sides by the heating on the feed side from the absorber-plate and a cooling cycle for the permeate side outside of the module, which constitutes the driving force instead of the vapor pressure difference created by the applied controllable vacuum in the VMD-FPC module in [6]. The cold distillate is used to be circulating on the permeate side, as a conventional DCMD configuration. The entire module is thermally insulated, same as a common FPC, to reduce heat loss to the environment. On the other hand, the solar radiation model in [6] was directly taken into the current study without any modification, obtaining the total received solar irradiance G_T, absorbed solar irradiance G_S (W m-

[2]). Coupled with the MD model, the final utilized solar energy G_u (W m^{-2}) can be acquired by deducting the top loss through the cover and the bottom loss from the thermal insulation.

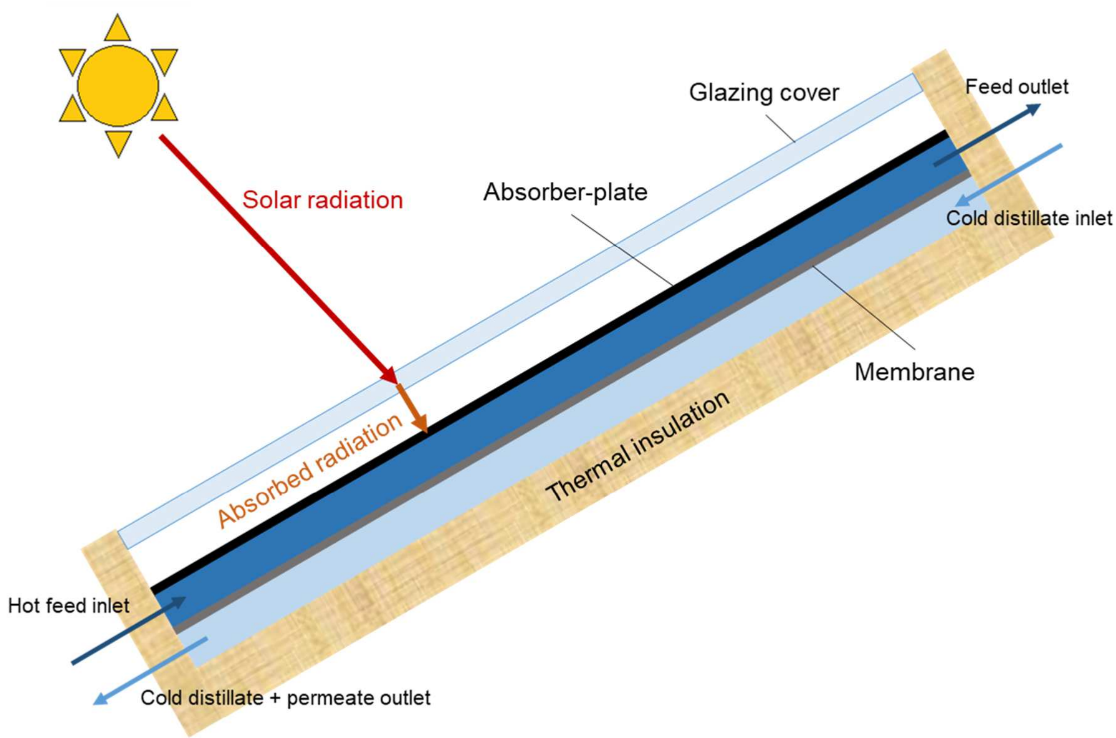

Figure 1: Configuration for an integrated DCMD-FPC module

2.2. Description of mass and heat transfer in MD modules

The governing equations consider the permeate vapor flux through the membrane, the heat transfer in the membrane, on the feed side and on the permeate side (temperature polarizations) and the salt diffusion on the permeate side (concentration polarization). The following main assumptions were applied in this study.

(i) a combined effect of Knudsen - molecular diffusion governing the mass transfer through the membrane in DCMD [4,34]; while a combined effect of Knudsen diffusion - viscous flow governing the mass transfer through the membrane in VMD [4,35];

(ii) steady state;

(iii) no wetting, crystallization or biofouling on the membrane;

(iv) a 100% salt rejection, thus no salinity on the permeate side;

(v) vaporization occurring only at pore inlet where the liquid-vapor interface holds;

(vi) thermal conduction through the membrane and boundary layer on the permeate side in VMD negligible due to the vacuum and no liquid existing on the vacuum side [5].

Based on Assumption (i), the diffusion coefficient used in [6] for VMD, which only considered Knudsen permeability K_m, is no longer applied here, and the contribution of viscous flow will be added and discussed. Furthermore, coefficients of the permeability for DCMD and VMD have to be respectively modeled based on membrane properties according to the above-cited mechanisms, which will be introduced in this section.

2.2.1. Transfer equations in DCMD

2.2.1.1. Heat transfer

Total heat flux through the membrane Q_p (W m^{-2}) is formulated as Eq. 1 [14], consisting of both the thermal energy for water evaporation taken away by the permeate flux J_w (kg m^{-2} s^{-1}), and the thermal conduction.

$$Q_p = J_w \Delta H_v + \frac{k_T}{\delta_m}(T_{fm} - T_{pm}) \tag{1}$$

where ΔH_v is the latent heat of water vaporization (J kg^{-1}), T_{fm} and T_{pm} the membrane surface temperature of the feed and the permeate side, δ_m the thickness of the membrane (m). k_T is the total thermal conductivity of the membrane layer (W m^{-1} °C^{-1}), which can be expressed by Eq. 2, applying the Isostress model [36].

$$k_T = \left(\frac{\varepsilon}{k_g} + \frac{1-\varepsilon}{k_p}\right)^{-1} \tag{2}$$

where ε represents the porosity of the membrane. k_p is the thermal conductivity of the membrane polymer part, while that of the gas (air and water vapor) trapped in the pore k_g can be estimated by the following correlation [37],

$$k_g = 2.72 \times 10^{-3} + 7.77 \times 10^{-5} T_m \quad (3)$$

On the other hand, the total heat flux Q_p is also transported through the boundary layers of the feed and the permeate side [38], which gives us the following,

$$Q_p = h_f\left(T_f - T_{fm}\right) = h_p(T_{pm} - T_p) \quad (4)$$

where T_f and T_p are the bulk temperatures. Due to temperature polarization, the former is higher than T_{fm} while the latter is lower than T_{pm}. h_f and h_p are the heat transfer coefficients (W m^{-2} $°C^{-1}$) of the feed and the permeate side, respectively.

The temperature polarization can be quantified by an important coefficient (TPC), as indicated in Eq. 5, representing how much the transmembrane temperature difference is reduced at membrane surface [39]. The closer to unity as TPC gets, the less impact of temperature polarization is implied.

$$\mathrm{TPC} = \frac{(T_{fm} - T_{pm})}{(T_f - T_p)}) \quad (5)$$

Correlations that correlate Nusselt number with Reynolds number Re and Prandtl number Pr are applied to the calculation of heat transfer coefficients. The ones proposed in [6] is adopted, which are as follows,

$$\mathrm{Nu} = 1.86\left(\frac{\mathrm{RePr}d_h}{L}\right)^{0.33}\left(\frac{\mu_f}{\mu_m}\right)^{0.14} \quad \text{for Re} < 2300 \quad (6)$$

$$\mathrm{Nu} = \frac{\left(\frac{f}{8}\right)(\mathrm{Re} - 1000)\mathrm{Pr}}{1 + 12.7\left(\frac{f}{8}\right)^{\frac{1}{2}}\left(\mathrm{Pr}^{\frac{2}{3}} - 1\right)}\left[1 + \left(\frac{d_h}{L}\right)^{\frac{2}{3}}\right]\left(\frac{\mathrm{Pr}_f}{\mathrm{Pr}_m}\right)^{0.11} \quad \text{for Re} \geq 2300 \quad (7)$$

With $f = (0.790 ln\mathrm{Re} - 1.64)^{-2}$

where d_h is the hydraulic diameter (m) and L is the length (m) of the flow channel. Dynamic viscosity μ (Pa s), density ρ (kg m^{-3}), thermal conductivity k (W m^{-1} °C^{-1}) and heat capacity c_p (J kg^{-1} °C^{-1}) of both saline water and distilled water are calculated by the regressions in [40].

2.2.1.2. Mass transfer

The water mass flux J_w (kg m^{-2} s^{-1}) is driven by the vapor pressure difference across the membrane due to the temperature difference [41],

$$J_w = B_m(P_{fm} - P_{pm}) \tag{8}$$

where B_m represents the overall membrane mass transfer coefficient (s m^{-1}), and P_{fm} and P_{pm} stand for the water partial pressure at the membrane surface on the feed side and the permeate side (Pa), respectively.

As described in the assumptions, B_m can be decomposed into the mass transfer coefficient in Knudsen diffusion B_K and the one in ordinary molecular diffusion B_D, which are calculated as follows,

$$B_K = \frac{2}{3}\frac{\varepsilon r}{\tau\delta_m}\left(\frac{8\mathrm{M}_w}{\pi \mathrm{R} T_m}\right)^{0.5} \tag{9}$$

$$B_D = \frac{\varepsilon}{\tau\delta_m}\frac{PD_w}{P_a}\frac{\mathrm{M}_w}{\mathrm{R}T_m} \tag{10}$$

where ε, r, τ, and δ_m are the porosity, the pore radius (m), the tortuosity and the thickness of the membrane (m), respectively. M_w is the molecular weight of water (kg mol^{-1}), and R is the gas constant (i.e. 8.3145 J mol^{-1} K^{-1}). T_m is the mean temperature (K) inside the membrane pore, P and P_a the total pressure and the air partial pressure (Pa) inside the membrane pore, and D_w the water diffusion coefficient (m^2 s^{-1}). It is worth to mention that the Knudsen permeability K_m utilized in [6] equals $B_K/\sqrt{\mathrm{M}_w}$.

Then the two mass transfer coefficients are combined by the following equation to obtain B_m [42],

$$B_m = (B_K^{-1} + B_D^{-1})^{-1} \tag{11}$$

Empirically, the product of the total pressure *P* and the water diffusion coefficient D_w can be calculated as a function of the temperature [14],

$$PD_w = 1.895 \times 10^{-5} {T_m}^{2.072} \tag{12}$$

Antoine equation is adopted for the calculation of pure water vapor pressure on each side of the membrane with the corresponding temperature at the membrane surface [4],

$$P^0 = \exp(23.1964 - \frac{3816.44}{T - 46.13}) \tag{13}$$

Then, the water vapor partial pressure on both side of the membrane has to take salt existence into consideration [4],

$$P = x_w \gamma_w P^0 \tag{14}$$

where x_w is the water molar fraction and γ_w is the water activity coefficient, which can be obtained by the correlation proposed in [40].

On the other hand, the permeate flux J_w is also determined by the water mass diffusion from the feed bulk to the membrane surface, which is further decided by the salt concentration polarization [43], yielding

$$J_w = \rho \lambda_m \ln\left(\frac{C_{fm}}{C_f}\right) \tag{15}$$

where λ_m is mass transfer coefficient (m s^{-1}) on the feed side, and *C* is the concentration (g L^{-1}). λ_m can also be estimated from the correlations given in Eqs. 6 and 7 by replacing Nusselt number Nu and Prandtl number Pr in the equations by Sherwood number Sh and Schmidt number Sc [44].

2.2.2. Modification of transfer equations in VMD

When compared with the VMD modeling at the scale of the module in [6], the only difference here lies in the diffusion mechanism inside the membrane pores, which is now the combination of Knudsen diffusion and viscous flow, instead of the assumption of solely Knudsen diffusion for the diffusion in VMD. The impact of this modification will be checked in Section 3.1.

Moreover, the diffusion coefficients need to be modeled from the material properties of the membrane, in order to be comparable with the DCMD model described above. Compared with Section 2.2.1, the modeling of VMD process takes 2 modifications into account. Firstly, the overall membrane mass transfer coefficient B_m is now composed of Knudsen diffusion B_K and the one in representing viscous flow B_V, which is calculated as [45],

$$B_V = \frac{M_w}{8\mu_v}\frac{\varepsilon r^2}{\tau\delta_m}\frac{P_m}{RT_m} \tag{16}$$

where μ_v is the viscosity of the vapor inside the pore, which can be calculated from the linearization from the data in [46].

B_m is the sum of these two coefficients,

$$B_m = B_K + B_V \tag{17}$$

The effect on the production of considering viscous flow will be discussed later to confirm the negligibility of B_V in VMD. Secondly, there is no more need to model the thermal conductivity of the membrane and the boundary layer on the permeate side, as explained in the assumptions. Therefore, the heat transfer becomes simply the heat transfer from the feed bulk to the membrane surface and the heat loss through membrane by vapor permeating, expressed as,

$$Q_p = h_f\left(T_f - T_{fm}\right) = J_w \Delta H_v \tag{18}$$

2.3. Description of the dynamic system

A recycling system was considered to not only fully store and exploit the solar energy absorbed by the module, but also to raise the water recovery rate to reduce the brine discharge of the system. For the VMD-FPC module, the VMD system design and dynamic modeling were already explicitly introduced and explained in [6], which included a recycling system on the feed side as well, and a vacuum pump directly connected to the permeate side. Therefore, Section 2.3 is dedicated to the description of the DCMD system for the DCMD-FPC module.

2.3.1. System configuration for DCMD-FPC module

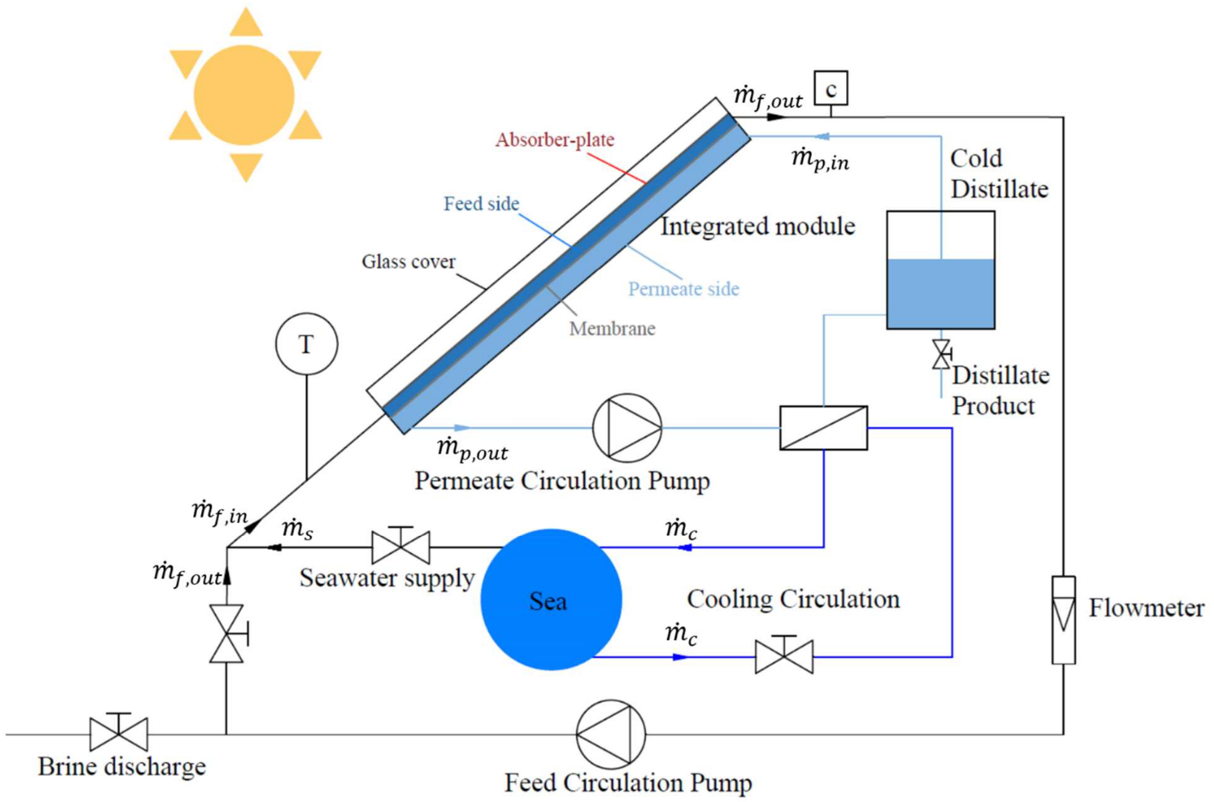

Figure 2: Flowsheet of recirculation system for DCMD-FPC module

Similar to the recycling batch system for the VMD-FPC module [6], the configuration of the system designed for the DCMD-FPC module is shown in Figure 2. Three water circulation loops function simultaneously, i.e. the feed recirculation, the cold distillate recirculation and the cooling seawater circulation. The feed stream absorbs thermal energy from the absorber-plate and induces higher vapor partial pressure, which generates vapor flux passing through the membrane pores when inside the module. The mass loss by permeate flux in the feed recirculation is compensated directly by the seawater supply instantaneously, while the whole feed side is evacuated by the discharge when the salt concentration gets too high and detected by the concentration meter at the outlet of the module. Counter-currently, the cold distillate on the permeate side gains the mass from the direct condensation of the vapor that passing through the membrane. However, thermal energy is also transferred to the circulation on the permeate side due to heat conduction through the membrane and permeate vapor condensation. Therefore, a cooling strategy for the cold distillate circulation is needed to substantially remove the additional heat delivered to the permeate side. Thus, the temperature of the distillate can be maintained lower than the feed, so that the transmembrane vapor pressure difference can be kept and the vapor inside the pores can be continuously condensed in the cold distillate due to the its higher pressure than the saturation pressure at the temperature of the permeate side. In the current configuration, the cooling of the permeate stream is realized by heat exchanging with the cooling seawater circulation, which constantly draws seawater at environment temperature from the sea.

2.3.2. System dynamics

The process dynamics was studied for time-varying steady-state phases [6]. Heat and mass balances were applied to both the feed side and the permeate channel, and salt mass conservation was used to track the accumulation of salt concentration.

Dynamics of the feed side are described by Eqs. 19 - 21. As aforementioned, mass loss to the permeate ($J_w A_m$) was made even by the seawater supply $\dot{m}_s$ (kg s^{-1}), which gives us Eq .19. Then, temperature change on the feed side was determined by the solar energy utilized G_u, supplied seawater and total heat loss through the membrane Q_p, yielding Eq. 20. Finally, salt mass kept augmenting during the process due to the no-salt-passing assumption and the salt introduction constantly from the seawater supply with a concentration of C_s (g L^{-1}), as presented in Eq. 21.

$$\frac{dm_f}{dt} = \dot{m}_s - J_w A_m = 0 \tag{19}$$

$$\frac{d(c_p m_f T_f)}{dt} = G_u A_m + c_p \dot{m}_s T_s - Q_p A_m \tag{20}$$

$$\frac{d(C_f V_f)}{dt} = \frac{C_s \dot{m}_s}{\rho_s} \tag{21}$$

where m_f is the total mass in the feed channel (kg), A_m is the surface area of the membrane (m^2) and V_f is the total volume of the feed channel (m^3).

On the other hand, the rate of mass gain in the distillate tank was all from the permeate ($J_w A_m$), and the temperature change was decided by the total heat transferred from the feed side Q_p and the heat taken away by the cooling circulation, as listed in Eqs. 22 and 23. A uniform temperature at any time was assumed for the fresh water inside the distillate tank T_d and the permeate side T_p of the module ($T_d = T_p$).

$$\frac{dm_d}{dt} = J_w A_m \tag{22}$$

$$\frac{d(c_p m_d T_d + c_p m_p T_p)}{dt} = Q_p A_m - Q_c A_c \tag{23}$$

where m_d and m_p are the total mass in the distillate tank and the permeate channel (kg), respectively. A_c and Q_c are the heat exchanging surface (m^2) and the heat flux taken away by cooling (W m^{-2}), which was solved by the "ht.hx" library in Python [47] for a counter-current heat exchanger.

2.4. Pumping energy consumption

The power consumption taken into consideration contains the consumption by circulation pumps (CP) in both DCMD-FPC and VMD-FPC systems and the additional consumption by a vacuum pump (VP) in the case of VMD-FPC. Due to the autonomous design of the system, thermal energy is entirely supplied by the available solar radiation on the surface of the MD-FPC module, which is more or less fixed with a given module at given location and time. While on the other hand, the power consumption for the system operation cannot be fulfilled by the module or the system itself, instead it requires external power supply from the grid, which is not often accessible in the targeted remote places and should be provided by on-site photovoltaic panels.

Consequently, it is worth to correlate the electricity demand to the production capacity of the desalination system.

2.4.1 Circulation pump

The electricity consumption of the circulation pumps is proportional to the pressure loss ΔP during the flow in the module, which consists of the friction loss and the gravitational loss due to the slope β of the module, neglecting the pressure loss in piping and joints. Therefore, the pressure loss in this study can be expressed as [44],

$$\Delta P = fL\frac{\rho v^2}{2d_h} + \rho gL\,\sin\beta \tag{24}$$

where L is the length of the module (m), v the flow velocity (m s^{-1}), and g the gravitational acceleration (9.81 m s^{-2}). f is the Darcy friction factor, being calculated by the correlations below [48,49].

$$f = \frac{96}{\text{Re}} \quad \text{for Re} < 2300 \tag{25}$$

$$f = (0.790\ln\text{Re} - 1.64)^{-2} \quad \text{for Re} \geq 2300 \tag{26}$$

Finally, the power consumption $\dot{P}_{cp}$ (W) of a circulation pump is [6]

$$\dot{P}_{cp} = \frac{F_V \Delta P}{\eta_{cp}} \tag{27}$$

where F_V is the volumetric flow rate (m^3 s^{-1}), and η_{cp} is the efficiency of the pump, which is taken as 0.7. In the system for the DCMD-FPC module, both the feed and the permeate circulation pumps were included in the calculation, while only feed circulation pump presented in the one for the VMD-FPC because of no permeate circulation existed. The pumping power from seawater source to both systems was excluded in the calculation, because it totally depends on the local seawater delivery arrangement and is out of the dynamic system design shown in Figure 2.

2.4.2. Vacuum pump in VMD system

A well-sealed system was assumed in this study, and thus the energy consumption by the vacuum pump is proportional to the amount of permeate vapor flux, according to the system configuration in [6], where all the vapor is pumped out by the vacuum pump. An isothermal compression from the vacuum pressure P_p to the atmospheric pressure P_{atm} is deemed more accurate to describe the process because of the relatively low permeate flow rate [50]. Accordingly, the power consumption $\dot{P}_{vp}$ (W) is

$$\dot{P}_{vp} = \left(\frac{J_w A_m}{\mathrm{M}_w \eta_{vp}}\right) \mathrm{R} T_p \ln\left(\frac{\mathrm{P_{atm}}}{P_p}\right) \tag{28}$$

where R is the ideal gas constant (8.31446 J mol^{-1} K^{-1}), and the efficiency η_{vp} equals 0.75 throughout the study. Here, the permeate temperature T_p is supposed to be the same as the temperature at the membrane surface on the feed side T_{fm} by the assumption of no conductive heat loss through the membrane.

2.5. Model coupling and resolution procedure

The system dynamics interacts with both the MD models and the solar radiation model, as shown in Figure 3. Operating conditions from the description of system dynamics (bulk temperatures, feed bulk concentration, flow rates) provided input parameters for MD model (Section 2.2) and Solar radiation model [6], while the results from both MD model and Solar radiation model imposed variations on operating conditions. During the simulation, the correlations for the calculation of mass & heat transfer coefficients and seawater properties were invoked by all these models.

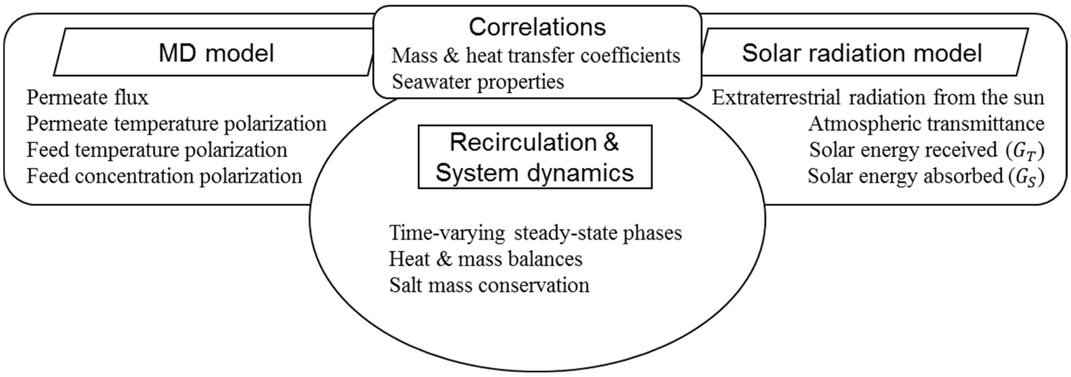

Figure 3: Schematic of interconnected modeling structure: MD model, solar radiation model and system dynamics

All models were programmed under Python (version 2.7). The integration for system dynamics (Eqs. 19 - 23) was realized by the Real-valued Variable-coefficient Ordinary Differential Equation solver (Isoda) in Scipy ODE package [51], in conjunction with the resolution of MD model (Section 2.2) and Solar radiation model by the Scipy fsolve package [52]. Automatic readjustments of time step-sizes and switches between the implicit Adams method for non-stiff problems and another method based on backward differentiation formulas (BDF) for stiff problems are provided by the Isoda package, in order to smoothly handle the integration.

3. Results and discussion

3.1. Parameter settings and daily operation

Concerning such an integrated module, different categories of parameters, i.e. location, material properties, positions & dimensions, and operating conditions, were included in the simulation. Table 1 presents an exhaustive list of all the parameters that intervened in the simulation.

The research was conducted in INSA Toulouse, thus the longitude, latitude and average altitude of Toulouse, France were chosen as an example for system operation and to give indications on the future experiments here in the laboratory. A 12-hour operation, from 8am to 8pm on Aug 1st was assumed, along with the daily ambient temperature varying from 20°C to 35°C and other parameters that affects the solar irradiance.

The properties of the glass cover, the absorber-plate, the membrane and the insulation were all taken into account as the 11 parameters in this category shown in Table 1. The first 5 parameters in material properties generally determine the amount of the solar energy absorbed from the received irradiance, and the other 6 parameters influenced how the module utilizes the energy input. The material properties other than the membrane were kept the same as listed in [6], while for the newly inserted membrane properties, the given data of the polyvinylidene fluoride (PVDF) membrane Durapore™ by Millipore was applied [53]. It is worth to note here that the tortuosity was set to a rather high value of 5 because of two reasons: (i) this value is much more difficult to evaluate compared to other membrane properties and is not given by the membrane manufacturer; (ii) more importantly, a tortuosity of 5 together with other membrane properties listed in the table corresponds to a Knudsen permeability of 5.74×10^{-6} s mol$^{1/2}$ m^{-1} kg$^{-1/2}$, which is at the same scope of the real values given by the experiments done in our laboratory [2]. Nevertheless, lower tortuosity values will be included in Section 3.3.2 by varying membrane properties.

Table 1: Parameter settings of integrated module and system for both DCMD-FPC and VMD-FPC

Parameters		Values	Description
Location & time	L_{loc}	358.56°	Longitude in degrees west, 0° < L < 360°
	φ	43.60°	Latitude, north positive, -90° < φ < 90°
	Al	150.0 m	Altitude of the location
	h_{wi}	10 W m^{-2} °C^{-1}	Heat transfer coefficient of the wind
	Date	Aug 1st	Date of the daily operation
	time	8 am - 8 pm	Duration of the daily operation
	r_0, r_1, r_k	0.97, 0.99, 1.02	Correction factors for mid-latitude summer
	ρ_g	0.2	Diffuse reflectance of the surroundings
	T_{amax}	35°C	Highest ambient temperature
	T_{amin}	20°C	Lowest ambient temperature
Material properties	n_c	1.5	Refractive index of the cover
	$K\delta_c$	0.032	Product of extinction coefficient and thickness
	ε_c	0.88	Emittance of the cover
	α_n	0.93	Absorptance in normal direction
	ε_{ap}	0.1	Emittance of the absorber-plate
	ε	0.713	Porosity of the membrane
	τ	5	Tortuosity of the membrane
	r	0.22 µm	Pore size of the membrane
	δ_m	117.7 µm	Thickness of the membrane
	k_p	0.15 W m^{-1} °C^{-1}	Thermal conductivity of the membrane polymer
	U_{bo}	0.9 W m^{-2} °C^{-1}	Heat loss coefficient of the insulation

Positions & dimensions	β	25.0°	Slope of the solar collector
	γ	0.0°	Azimuth angle of the solar collector
	W	0.5 m	Width of the collector
	L	0.7 m	Module length
	δ_f	5 mm	Thickness of the feed side
	δ_p	5 mm	Thickness of the cold distillate side (only DCMD)
Operating conditions	C_s	35 g L^{-1}	Salt concentration of the seawater supply
	T_s	25°C	Temperature of the seawater supply
	C_{limit}	300 g L^{-1}	The highest operating salt concentration
	$\dot{m}_f$	100 kg h^{-1}	Feed circulation flow rate
	$\dot{m}_p$	100 kg h^{-1}	Permeate circulation flow rate (only DCMD)
	$\dot{m}_c$	150 kg h^{-1}	Cooling circulation flow rate (only DCMD)
	m_d	5 kg	Initial mass in the distillate tank (only DCMD)
	U_c	1000 W m^{-2} $°C^{-1}$	Cooling heat exchange coefficient (only DCMD)
	A_c	0.1 m^2	Cooling heat exchange surface (only DCMD)
	P_p	5000 Pa	Permeate pressure (only VMD)

It is also worth noting that in the positioning angles and the dimensions of the flat-plate module, the collector area ($W \times L$ = 0.5m × 0.7m) of both DCMD-FPC and VMD-FPC modules was considered the same as the membrane area A_m, because they shared the same surface in the integrated design, neglecting edges and margins. Besides, in VMD the thickness and the flow rate of permeate side was excluded due to the total vapor phase inside the vacuum on the permeate side, which was assumed to be a uniform vacuum pressure at 5000 Pa. Contrarily for the DCMD-based system, the same thickness and flow rate as the feed side for the permeate side was taken. Rather low flow rates at 100 kg h^{-1} (corresponds to a Re of around 130) were initially taken based on the conclusion that lower flow rate is beneficial to the performance of solar-driven DCMD [14]. Similarly, the flow rates will be later varied in a large range to see their impact on the system performance. A distillate mass of 5 L was assumed to be already in the cold distillate circulation before the daily operation, to initiate the permeate circulation.

The considered seawater source had a constant concentration of 35 g L^{-1} and a constant temperature of 25°C. The limit of salt concentration before discharge in the module was set to be a higher value of 300 g L^{-1}, giving a maximal water recovery rate of 88.3%. Specifically for the DCMD-FPC, a small heat exchanger of 0.1 m^2 for cooling the permeate was set, whose overall heat transfer coefficient was 1000 W m^{-2} K^{-1}, as a normal liquid-liquid plate heat exchanger [54]. The cooling seawater circulated at a flow rate of 150 kg h^{-1}, more than the flow rate of the cold distillate to ensure a good cooling effect. All the above settings for the cooling cycle would be later varied to discuss their influences.

Under the settings of all the parameters listed in Table 1, simulations for the DCMD-FPC system and the VMD-FPC system were performed, resulting in daily variations of solar irradiance, temperatures, TPC, concentrations and permeate fluxes as shown in Figure 4.

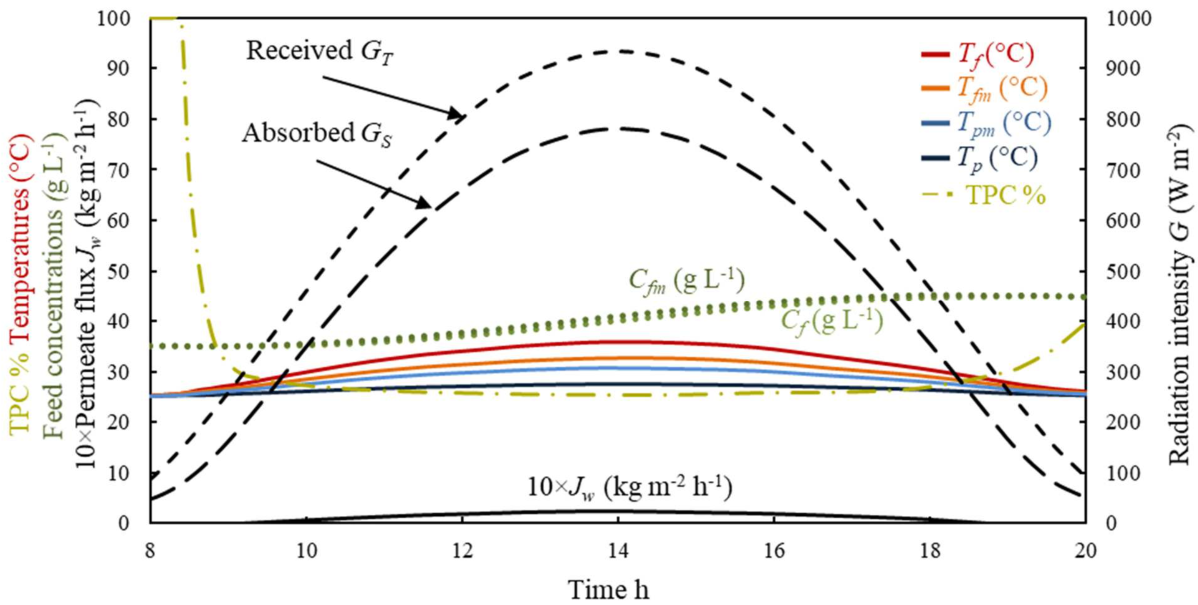

(a)

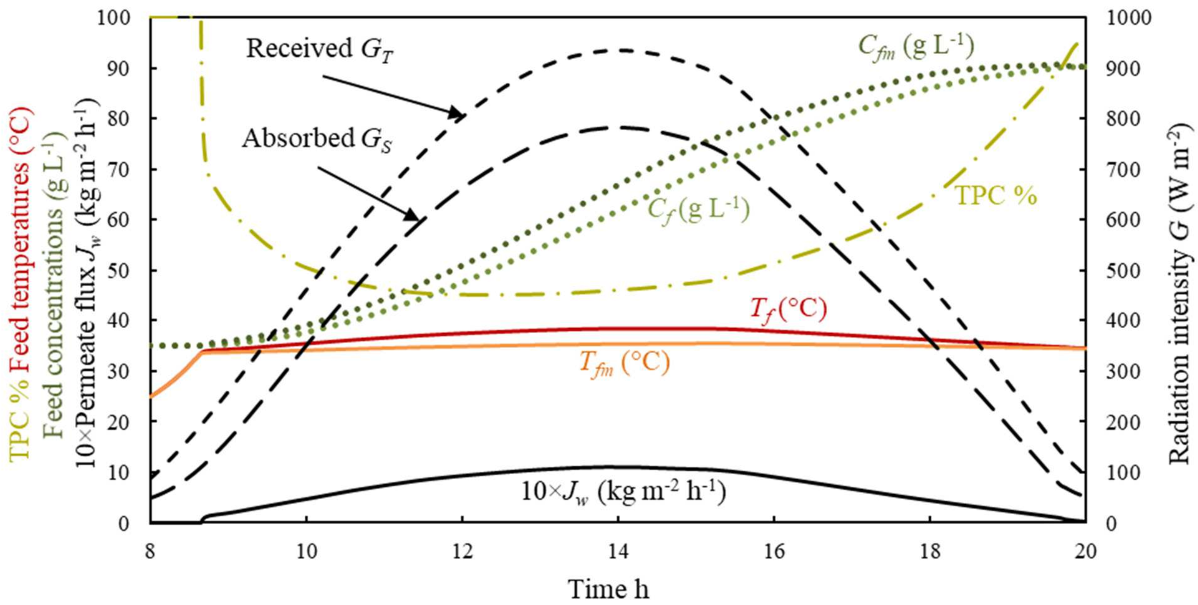

(b)

Figure 4: Daily variation of solar irradiance, feed and permeate temperature, TPC, feed concentration and permeate flux of (a) DCMD-FPC system; (b) VMD-FPC system

Similarity between Figure 4a and 4b was observed for all the variations. Received solar irradiance G_T is exactly the same in both of the figures because of the same date and location chosen, and the absorbed irradiance G_S also seems to be nearly the same. The operating temperatures and permeate fluxes all rise a bit with the increment of solar irradiation and all go down with the decreasing solar condition in the afternoon. Besides, both of the concentrations kept accumulating as shown in Figure 4, and the slope is bigger when near noon because of relatively higher permeate flux under stronger solar radiation. At the same time, TPC and concentration polarizations (differences between C_{fm} and C_f) of both systems are more obvious with higher permeate flux at noon. Specifically for the DCMD-based system, the temperature of the bulk on the permeate side T_p did not react too much to other variations due to the cooling effect impeding it from augmenting. As for the VMD-based system, the feed temperature started at the original 25°C in the beginning of the day and then was raised to a certain point before being more or less stabilized, when the water vapor pressure on the feed side reached the level of the vacuum pressure and permeate flux began to appear.

Despite the similar variations, the difference on the production was obvious. After the day, the VMD system can produce 8.08 kg m^{-2} of distillate water (2.83 L), while the DCMD-FPC module will produce only 1.46 kg m^{-2} (0.51 L). Therefore, the permeate flux in Figure 4b is much higher than that in 4a, even though it is already rather low. Even though the temperature polarizations ($T_{fm} < T_f$) on the feed side seem to be in the same range for both DCMD-FPC and VMD-FPC, the extra temperature polarization on the permeate side ($T_{pm} > T_p$) for DCMD-FPC significantly exacerbates TPC to as low as 26%, and hence further reduces permeate flux. As a result, the salt concentration C_f of the VMD-FPC system accumulated much more than the DCMD-based system because of more water permeated, and its concentration polarization phenomenon is stronger compared to the nearly-invisible difference between C_f and C_{fm} in Figure 4a. However, the difference in power consumption for these two systems was even more significant. The DCMD-FPC system produced the distillate at an expense of only 2.76×10^{-3} kWh (average PV power consumption 0.23W, corresponding SEEC 5.42 kWh m^{-3}), while the value for the VMD-FPC system was 0.45 kWh (average PV power consumption 37.5W, corresponding SEEC 158.4 kWh m^{-3}), most of which was consumed by the vacuum pump, because of the configuration of the VMD system where vacuum pump was used to compress all the produced water vapor. This important consumption is inevitable, and can be seen as the replacement of the huge expense on maintaining an extremely low temperature in "cold traps", which is usually installed before the vacuum pump to condense vapor in vacuum. On the other hand, the total absorbed solar energy for both systems recorded about 2 kWh during the 12-hour operation. Considering a latent heat of vaporization of 2260 kJ kg^{-1} [55], the DCMD-based system only utilized 0.32 kWh out of the 2 kWh (16% thermal efficiency) for water production, while the VMD-based system transferred as much as 1.78 kWh into the final distillate (89% thermal efficiency). In conclusion, significantly higher electricity consumption and solar energy utilization efficiency both existed for the VMD-FPC, compared to the DCMD-FPC.

In addition, the assumptions of mass transfer mechanisms inside the membrane pore are revisited here by some extra simulations. For DCMD, the daily production would be 106.9% higher if only considering Knudsen diffusion instead of a combined effect of Knudsen-molecular diffusion; while it would be 18.3% higher if only molecular diffusion is considered. Therefore, this combined Knudsen-molecular diffusion is necessary for better prediction of the permeation, without the need of including viscous flow due to the existence of air. For VMD, molecular diffusion does not exist due to the vacuum and no air. The daily production would only be 0.06% lower if viscous flow is further excluded and only Knudsen diffusion is assumed to govern the transfer inside the pores. Therefore, it confirms the assumption that solely Knudsen diffusion is already enough to describe the transfer mechanism of VMD.

3.2. Comparison of simplified cost of water (SCOW)

From a techno-economic view, the simplified cost of water (SCOW) is adapted here [56,57], in order to incorporate both the production and the energy consumption metrics into one comparable desalination performance indicator. It is worth noting that such a criterion might not be the only factor that determines the applicability of the studied small-scale solar-driven desalination device. For example, process robustness and sustainability are probably more important aspects that have to be considered when implementing such distributed devices in remote places without consistent energy supply. However, these additional factors are hard to evaluate in the current simulation study, and will be further discussed in our future experimental research.

In Toulouse, the annual insolation time is around 2040 hours with a total received solar radiation energy of 5924 MJ m^{-2} at an optimal slope [58]. Based on such a solar condition, a discount rate i of 7% and a nominal escalation rate r of 4% are assumed upon a system lifetime of 20 years [56,59]. The detailed SCOW calculation chart is listed in Table 2 for a solar collecting area of 1 m^2, including all the reasonable cost assumptions. All the costs are in euros €.

It is obvious that both devices are still more expensive compared with large-scale desalination facilities [60], due to the rather low production rates of the current system layouts without heat recovery or any other performance optimizations (potential production capacities will be discussed in Section 3.4). However, this techno-economic calculation is just a first estimation of water producing cost for the essential drinking water provision in some water-deficient remote area, and comparing this cost to the price of bottled water (~ 0.5 € per liter in Europe) might be more relevant. Between DCMD-FPC and VMD-FPC, not only the production rate of the latter (8.08 kg m^{-2}) is much higher than the former (1.46 kg m^{-2}), but also the SCOW of the latter (0.10

€ L^{-1}) is considerably lower than the former (0.17 € L^{-1}), despite the additional cost of vacuum pump and electricity consumption.

Table 2: Cost calculation and SCOWs of DCMD-FPC and VMD-FPC without heat recovery

<table>
<tr><th>Item</th><th>Description</th><th>Cost (DCMD-FPC)</th><th>Cost (VMD-FPC)</th></tr>
<tr><td>C_I</td><td>Total investment costs, $C_{eq} + C_{con}$</td><td>360</td><td>600</td></tr>
<tr><td>C_{eq}</td><td>Equipment costs, $C_{MD} + C_{HX} + C_{rMD}$</td><td>300</td><td>500</td></tr>
<tr><td>C_{con}</td><td>Construction costs, 0.2 x C_{eq} [56]</td><td>60</td><td>100</td></tr>
<tr><td>C_{MD}</td><td>MD module costs, $C_{memb} + C_{matMD}$</td><td colspan="2">100</td></tr>
<tr><td>C_{memb}</td><td>Membrane costs</td><td colspan="2">50</td></tr>
<tr><td>C_{matMD}</td><td>Module material costs other than membrane</td><td colspan="2">50</td></tr>
<tr><td>C_{HX}</td><td>Heat exchanger costs</td><td colspan="2">100</td></tr>
<tr><td>C_{rMD}</td><td>Other module costs (piping, pumps, etc.)</td><td>100</td><td>300</td></tr>
<tr><td>C_F</td><td>Operational costs, $C_{SM} + C_{IN} + C_{RMD}$</td><td>23.3</td><td>30.5</td></tr>
<tr><td>C_{SM}</td><td>Service and maintenance costs, 2.5% x C_I [61]</td><td>9</td><td>15</td></tr>
<tr><td>C_{IN}</td><td>Insurance costs, 0.5% x C_I [62]</td><td>1.8</td><td>3</td></tr>
<tr><td>C_{RMD}</td><td>Membrane replacement costs, C_{memb} x 1/4, [63]</td><td colspan="2">12.5</td></tr>
<tr><td>C_V</td><td>Variable operational costs, $C_{CH} + C_{EL} + C_{TH}$</td><td>0.24</td><td>35.40</td></tr>
<tr><td>C_{CH}</td><td>Chemical costs, € 0.038 m^{-3} [64]</td><td>0.02</td><td>0.12</td></tr>
<tr><td>C_{EL}</td><td>Electricity costs, € 0.103 kWh^{-1} [65]</td><td>0.22</td><td>35.28</td></tr>
<tr><td>C_{TH}</td><td>Thermal energy costs, 0 due to solar-heating</td><td colspan="2">0</td></tr>
<tr><td>SCOW</td><td>Simplified Cost of Water, € L^{-1}</td><td>0.17</td><td>0.10</td></tr>
</table>

3.3. Influence of parameters

In order to examine the individual influence of some parameters on the performance, the value of each parameter was varied one-at-a-time (OAT) while keeping all the other parameters the same as listed in Table 1 as a module of $0.5\times0.7m^2$. The performance observations are based on the same daily production D_p and SEEC. The studied parameters include the material properties of solar absorption and the membrane, the operating conditions, and the module position and dimensions, which are presented and discussed as follows.

3.3.1. Solar oriented material properties ($A_m = A_c = 0.5\times0.7m^2$)

The main solar oriented material properties that exert influence on system operation include the properties of the glass cover (n_c and $K\delta_c$) and the absorptance α_n in normal direction of the absorber-plate. These parameters characterized the solar energy absorption of the module, being the only thermal energy source of the system.

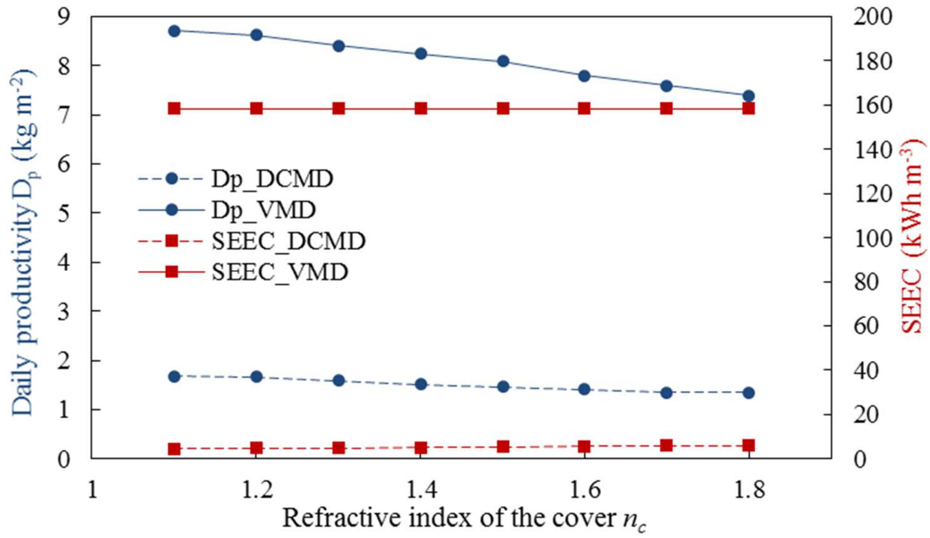

(a)

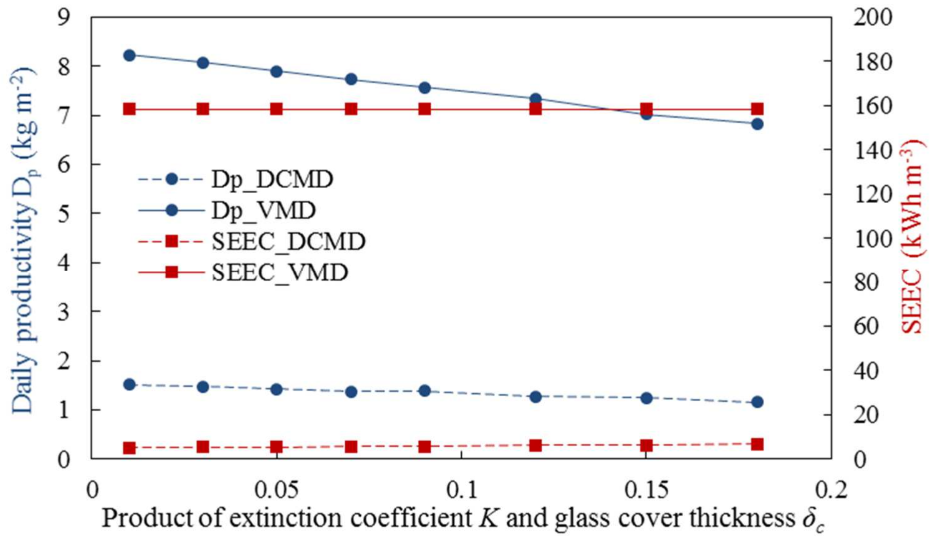

(b)

Figure 5: Daily distillate productivity and specific electrical energy consumption for DCMD-FPC and VMD-FPC systems at varying glass cover properties: (a) refractive index n_c; (b) product of extinction coefficient K and thickness δ_c

The first layer of the integrated module is the glass cover. As expected and shown in Figure 5, increasing the values of the concerned properties had bigger negative impact on the daily distillate production D_p for the VMD-based system than the DCMD one. The VMD-FPC system was much more productive than the DCMD-FPC, with specific consumption unaffected by the properties of the glass cover. However, the SEEC of the DCMD-based system varied a little bit with different values of these properties, though not clear in these figures because of much smaller value compared to the value of VMD. It increased from 4.7 to 5.9 kWh m^{-3} with n_c being from 1.1 to 1.8, and from 5.2 to 6.8 kWh m^{-3} with $K\delta_c$ being from 0.01 to 0.18. The circulation flow rates are fixed in these calculations and thus the total pumping consumption remained the same while D_p decreased with the increments of these properties. As a result, the specific consumption of the DCMD-based system raised when bigger n_c or $K\delta_c$ were imposed.

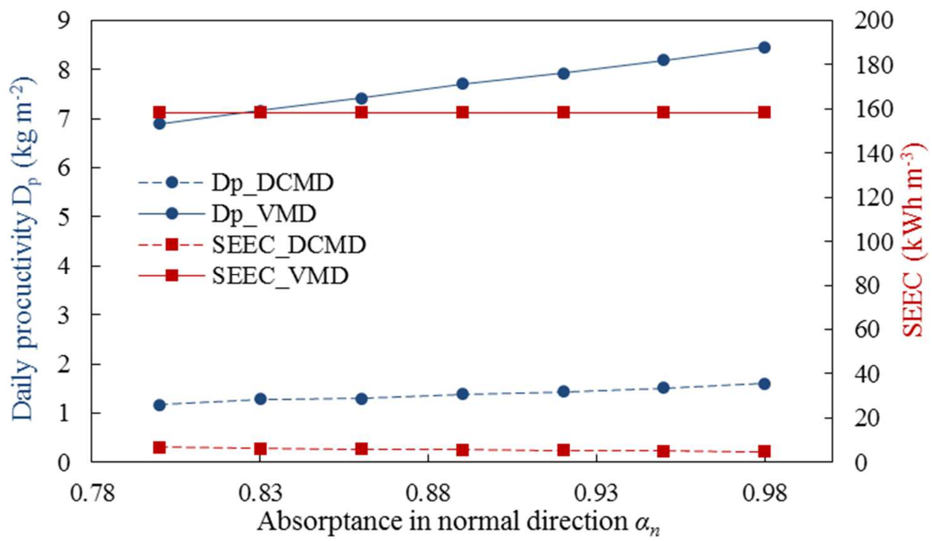

Figure 6: Daily distillate productivity and specific electrical energy consumption for DCMD-FPC and VMD-FPC systems at varying absorptance α_n in normal direction of absorber-plate

Similar observations of the absorptance α_n of the absorber-plate is shown in Figure 6. However, the absorptance α_n had a positive impact on D_p for both MD configurations, based on the fact that higher absorptance directly enabled greater amount of the solar energy absorbed. On the other hand, D_p of the DCMD-FPC system stayed limited at 1.60 kg m^{-2} even with the highest absorptance, while SEEC ranged from 6.75 kWh m^{-3} with α_n at 0.8 to 4.95 kWh m^{-3} with α_n at 0.98, whose variation was also limited. Compared to the positive impact of α_n on the production of the VMD-FPC, the strong conductive heat loss through the membrane in DCMD-FPC might severely diminished the benefit from higher solar absorption.

3.3.2. Membrane properties ($A_m = A_c = 0.5 \times 0.7 m^2$)

For both DCMD-based and VMD-based desalination systems, four characteristic membrane properties were considered, that is to say porosity ε, tortuosity τ, thickness δ_m and pore size r, as they characterize the membrane permeability and decide the mass transfer quality of the separation process. Influence of these properties on the performance of both modules are summarized in Figure 7, together with the corresponding Knudsen permeability of the membrane.

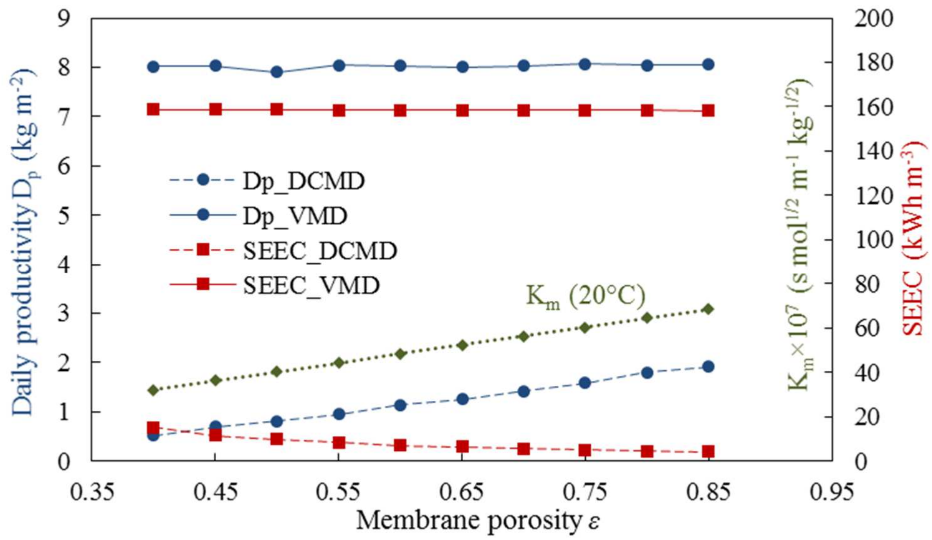

(a)

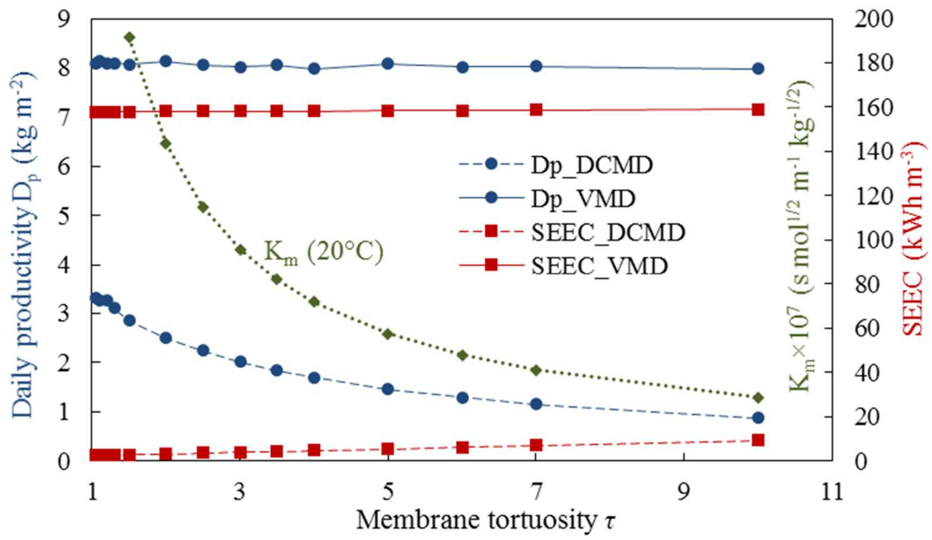

(b)

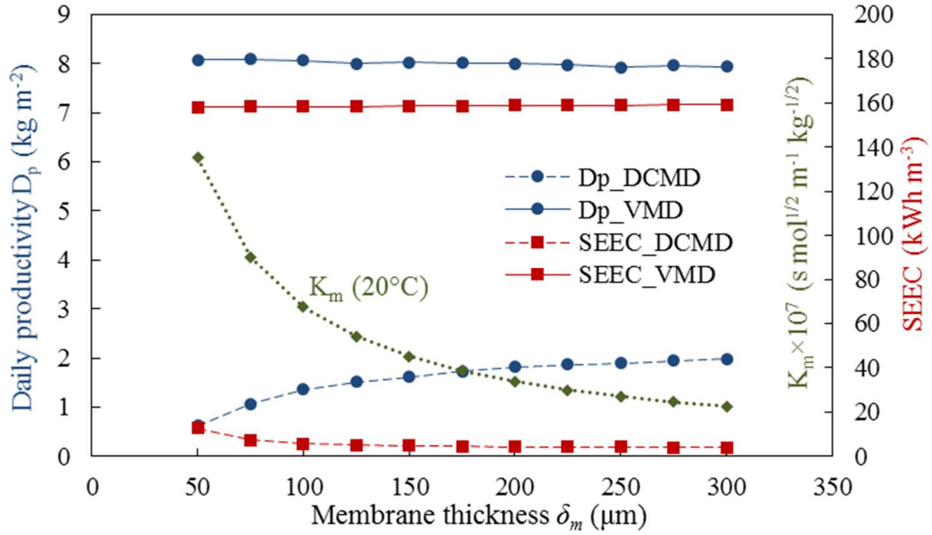

(c)

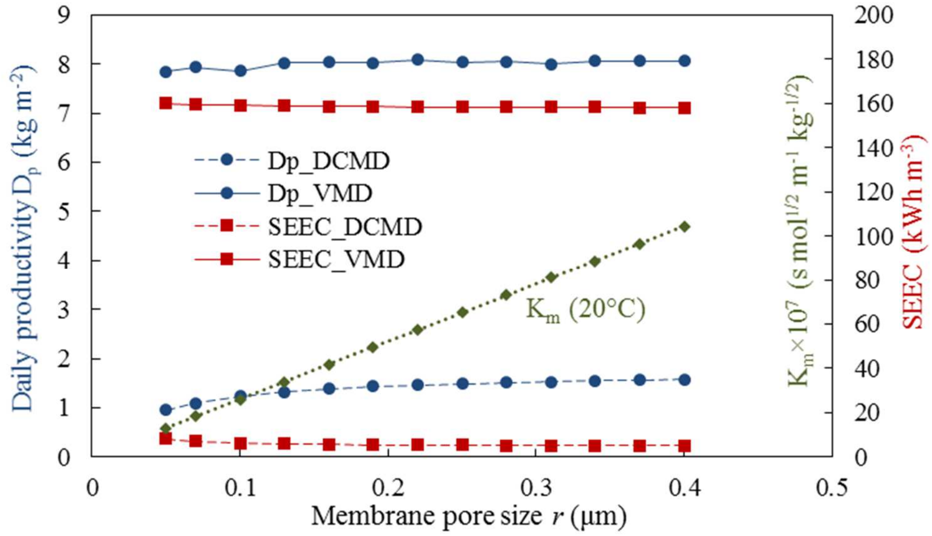

(d)

Figure 7: Daily distillate productivity and specific electrical energy consumption for DCMD-FPC and VMD-FPC systems at varying membrane properties: (a) porosity ε, (b) tortuosity τ, (c) thickness δ_m, (d) pore size r

Clearly, these permeability-oriented parameters had very small influence (almost no influence) on the water production and pumping consumption of the VMD-based system, the same as previously discussed for the Knudsen permeability K_m of the membrane due to the restraining from limited solar energy income. Oppositely, both the D_p and the SEEC of the DCMD-based system acted sensitively to membrane properties, which indicates that the sparse solar radiation is not the only constraint in DCMD-FPC. Higher porosity and lower tortuosity seemingly benefited the system a lot with greater production and less pumping consumption, because of the enhanced permeability of the membrane, as the K_m shown in Figure 7a and 7b, which increases linearly with higher porosity and exponentially with lower tortuosity. A low tortuosity of 1.2 could push D_p up to 3.3 kg m^{-2}, which however seemed to be the limit for even lower tortuosity (same D_p of 3.3 kg m^{-2} with τ of 1.05). Similarly, the larger pore size was able to do the same job of boosting the production, but only to a limited extent. Larger than an average pore size of 0.3 μm, no clear improvement on the system performance is visible at an increasing pore size even though the Knudsen permeability keeps rising linearly, and the risk of membrane wetting would be significantly increased. Lastly, thicker membranes in the case of DCMD-FPC were found to be of interest to both D_p and SEEC, even it induced lower membrane permeability. The reason is that by increasing the membrane thickness, another important factor, the conductive thermal loss, came into play. The thicker the membrane, the bigger thermal resistance of this layer. Therefore, this observation proved that reducing transmembrane conductive heat loss and increasing the thermal efficiency in the DCMD-FPC system are more important than enhancing membrane permeability.

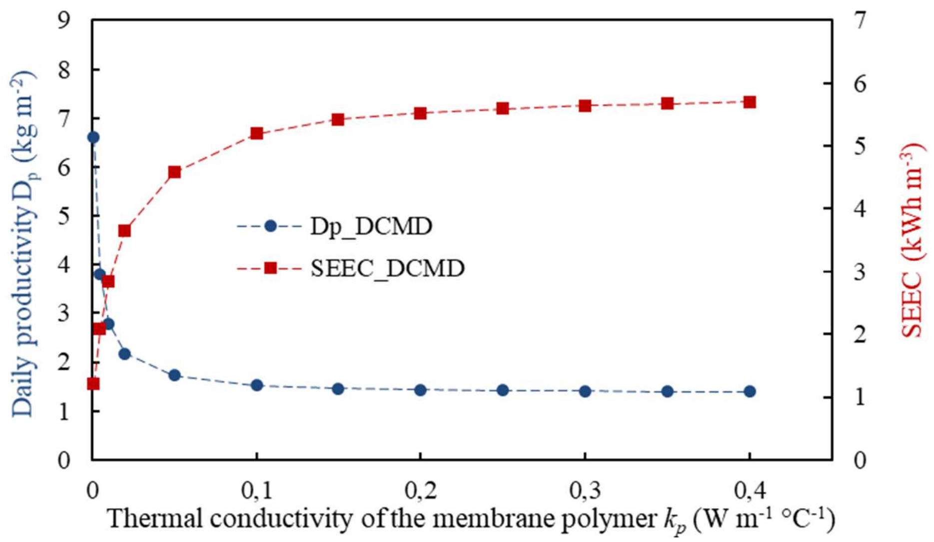

Figure 8: Daily distillate productivity and specific electrical energy consumption for the DCMD-FPC system at varying thermal conductivities k_p of membrane polymer

Having in mind that the conduction thermal loss of the membrane might be essential to the DCMD-based system, the thermal conductivity of the membrane polymer k_p is therefore analyzed here in Figure 8. The VMD-based system was not taken into consideration because of the neglected conductive loss through the membrane.

As expected and discussed above, the production of DCMD-FPC responded a lot to this parameter, which could even reach up nearly to the D_p of the VMD system with extremely low thermal conductivity. Therefore, the conductive heat loss can be identified as the dominant factor that caused the large production difference between DCMD-based and VMD-based system. Besides, SEEC exhibits an inverse trend compared to the trend of D_p, because of the invariability of the total pumping consumption at fixed flow rates of the feed and the distillate, which is the product of SEEC and total water produced. However in reality, the thermal conductivity of the membrane is still in the range from 0.15 to 0.30 W m^{-1} K^{-1} (0.17 for PP, 0.19 for PVDF and 0.25 for PTFE) [66], where there seemed no significant influence on system performance from Figure 8.

3.3.3. Operating conditions ($A_m = A_c = 0.5 \times 0.7 m^2$)

Firstly, the permeate pressure P_p was again identified to be the major factor determining the performance of a VMD-FPC system, same as reported previously [6]. Then, the flow rate of the feed recirculation $\dot{m}_f$ for both DCMD-FPC and VMD-FPC and the flow rate of the cold distillate recirculation $\dot{m}_p$ for DCMD-FPC are discussed as follows. In order to be more interpretable, instead of flow rates, the corresponding average Reynolds number were illustrated in Figure 9.

For the VMD-based system, higher Reynolds number of the feed did not end up with higher D_p due to the limited available solar energy, only adding slightly to the energy consumption of pumping [6]. From Figure 9, similar behaviors can be observed for DCMD-based system, where an almost constant D_p is observed in spite of the varying Reynolds numbers of the feed or the permeate side. Apart from the same limitation by the incoming solar energy as for VMD-based system, here the conductive heat loss account for another important constraint, as discussed in Section 3.3.2.

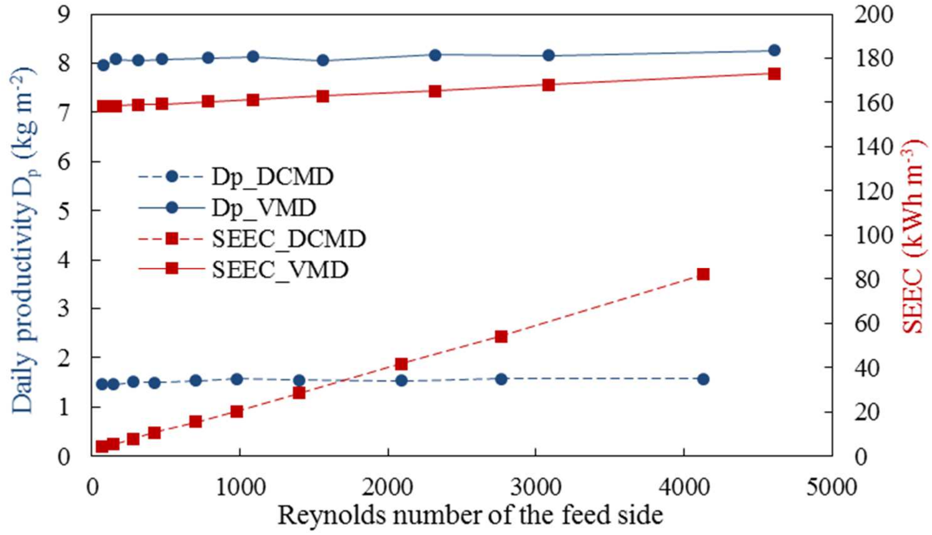

(a)

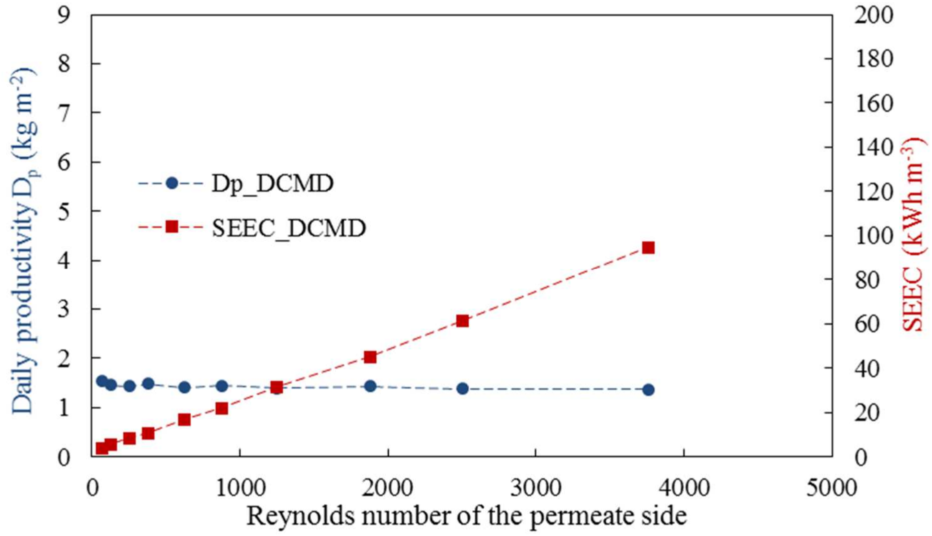

(b)

Figure 9: Daily distillate productivity and specific electrical energy consumption at varying Reynolds numbers: (a) feed side for both DCMD-FPC and VMD-FPC modules; (b) permeate side for DCMD-FPC module only

On the other hand, the pumping consumption of DCMD-FPC were nearly proportional to the Reynolds number (from 2 Wh at a Re around 70 to 45 Wh at Re around 4000) because of the linear relation between the power consumption of CP and the flow rate, as expressed in Eq. 27, and no other electricity consumptions taken into account. Then, due to the unchanged D_p, SEECs of the DCMD-FPC in Figure 9 also increases linearly with Re of either the feed flow or the cold distillate circulation. While for VMD-FPC, the majority of the pumping consumption was taken up by the consumption of the vacuum pump. At a low Re of the feed flow (Re < 500), over 99% of the total consumption was found out to be spent on VP. Even when the feed flow was at the highest Re of 4600 in Figure 9a and the consumption by CP would be at its maximum, 0.46 kWh was consumed by VP, out of the total consumption of 0.50 kWh, leaving only 44 Wh consumed by the CP of the feed circulation. Then, the power consumption of VP is proportional to the amount of permeate vapor and not influenced by the feed flow rate, according to Eq. 28. Therefore, the major part of the SEEC of VMD-FPC in Figure 9a that belongs to the vacuum pump stayed constant due to the constant D_p. For the rest that consumed by CP in VMD-based system, its total amount increased with the Re at the same pace as the DCMD-based system. However, the total SEEC (by VP and CP) of VMD-FPC in Figure 9a ascends more slowly with the increasing feed Re than the ascending pace of the SEECs of DCMD-FPC, which is because of the greater production in VMD-FPC incurring lower specific consumption by CP and thus smaller slope of the total SEEC.

Regarding the water productivity D_p for DCMD-FPC, in fact, it increased slightly from 1.45 to 1.58 kg m^{-2} with feed Re from below 100 to about 4000, while it decreased from 1.55 to 1.37 kg m^{-2} with permeate Re from below 100 to nearly 4000. This observation further backs up the important impact of transmembrane conductive thermal loss in DCMD. Higher feed Re can help to enhance the heat transfer from the feed bulk to the boundary layer to provide for water evaporation and heat conduction through the membrane. However, higher permeate Re helped to improve the reception of not only water condensation heat but also conductive heat loss by enhancing heat transfer from the permeate boundary layer to the bulk. In consequence, the higher permeate Re permitted larger overall heat loss from the limited solar energy input and caused the declination of D_p. Conclusively, higher Re of both the feed and the permeate side contributes to higher pumping consumption without enhancing the productivity of the DCMD-FPC, therefore lower Re is more favorable for this simple recirculation system, same as concluded for VMD-FPC in case no heat recovery strategy was implemented [6].

Beside the feed and permeate recirculation, a cooling cycle is involved also in the system as illustrated in Figure 2, where seawater source is circulating and cooling the permeate recirculation. The concerned parameters are the cooling flow rate $\dot{m}_c$, the heat exchange coefficient U_c and the heat exchange surface A_c, and the latter two intervene the model by their product U_cA_c. Figure 10 presents their impact on the system performance of DCMD-FPC module.

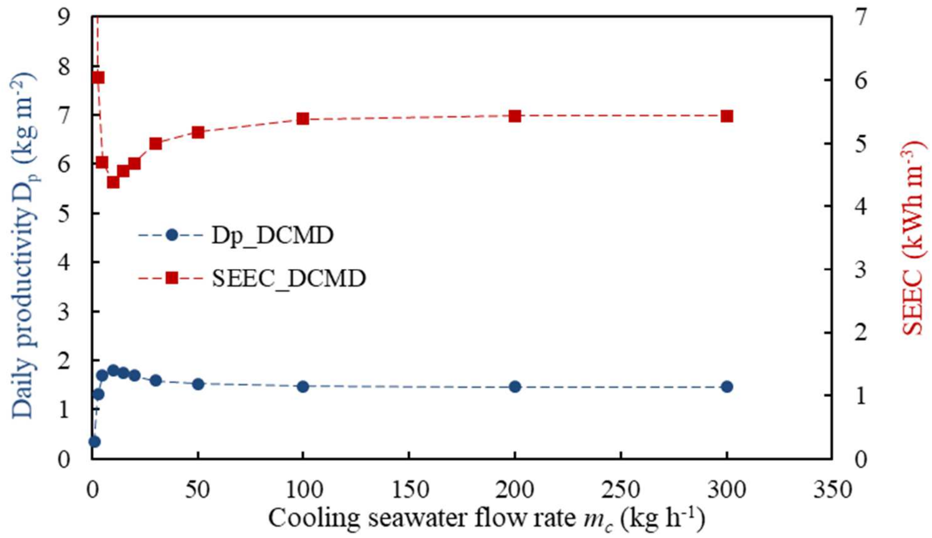

(a)

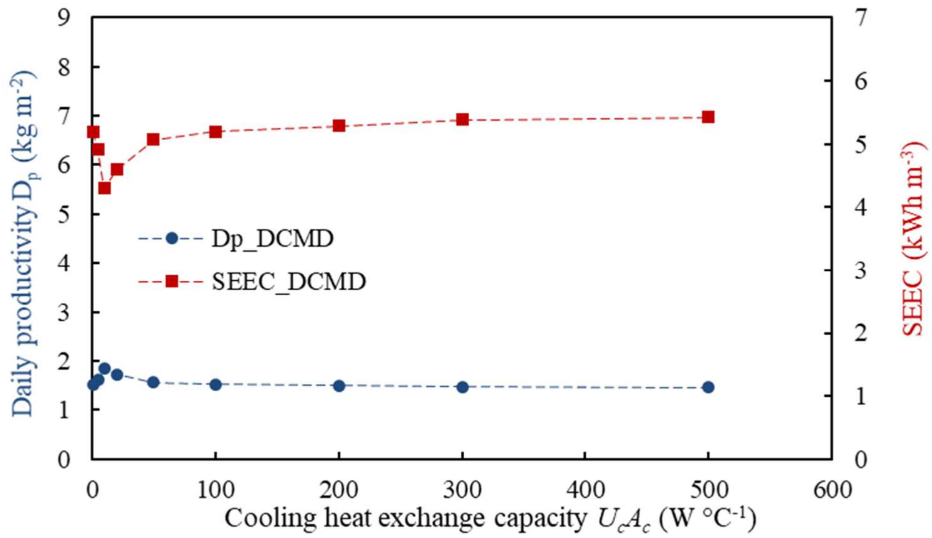

(b)

Figure 10: Daily distillate productivity and specific electrical energy consumption at varying: (a) cooling circulation flow rate $\dot{m}_c$, (b) cooling heat exchange capacity U_cA_c

Both very low values of $\dot{m}_c$ and U_cA_c were preferred by the DCMD-based system, being around 10 kg h^{-1} and 10 W K^{-1}. However, the possible improvement by adjusting the cooling condition was still very limited compared to altering membrane properties as discussed in Section 3.3.2. Furthermore, this preference again confirms the strong influence of heat conduction through the membrane. Better cooling effect can ensure a lower temperature of the cold distillate on the permeate side, which strengthens the driving force and thus the permeate flux. On the other hand, such lower temperature can induce bigger transmembrane conductive heat loss. Therefore, the low values of the optimal choice indicated that, for the same module configuration, more emphasis should be put on reducing heat conduction in DCMD instead of enhancing the production. Besides, the variations of SEECs in Figure 10 are due to the variations of the production, while the total consumption, taken the CPs on the feed and the permeate was not affected at all by the cooling condition.

3.3.4. Module position and dimensions

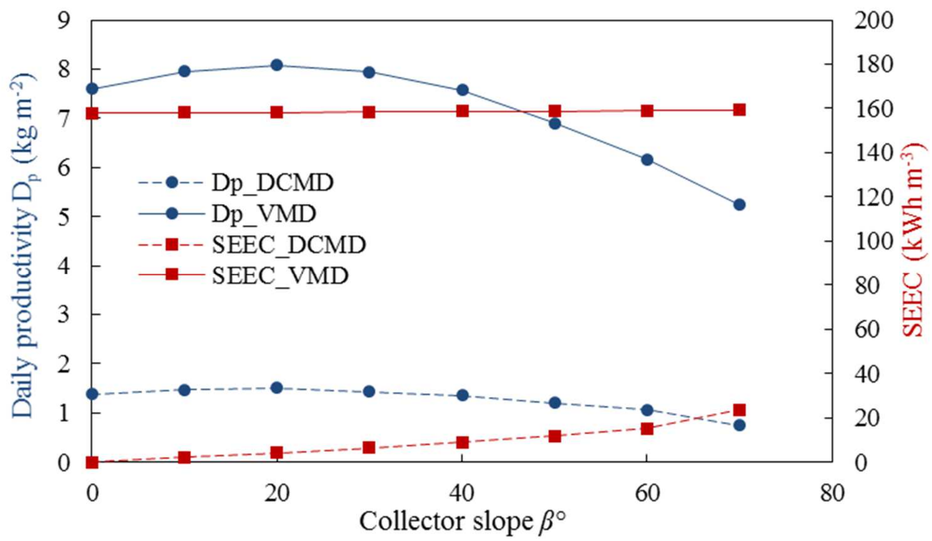

Figure 11: Daily distillate productivity and specific electric energy consumption at varying slope

Firstly, the module position was fixed by the slope β and the azimuth angle γ. The latter is usually set to 0, facing sharply south, for non-tracking non-concentrating solar collectors to maximize the received energy on the surface. Hence, the position parameter in question is the inclination of the module. D_p of both systems exhibited a same favorite slope at around 20°, as shown in Figure 11. However, the pumping consumption behaved differently. Theoretically, bigger slope added to the burden of circulation pumps to overcome greater pressure difference between the bottom and the top of the module due to the elevated module height. Thus, both of the feed pump and the permeate pump had to consume more at bigger inclination in the DCMD-FPC system, while the improvement of water production from 0° to 20°C was limited. The specific consumption of the VMD-FPC system, on the other hand, seldom reacted to the variation of the slope because the majority of the consumption was taken up by the vacuum pump.

Secondly, the dimensions of the MD module consisted of the module length *L*, the module width *W* and the thicknesses of feed δ_f and permeate δ_p. In the VMD-based module, there would be no discussion on the thickness of the permeate side because of the assumption of a uniform vacuum space without water circulation. The influences of the dimensions on the performance of both DCMD-FPC and VMD-FPC are illustrated in Figure 12.

The length of the module hardly altered the performance of both systems. With very limited thermal energy input from the absorber-plate, the total water volume and the heat and mass transfer inside the channel, which were connected with the length, did not seem to be influential. Similarly, no clear influence of the module's width was observed except for the SEEC of the DCMD-based module. This observation was due to the augmenting flow velocities and Reynolds numbers on both sides of the membrane, when decreasing the module width under fixed flow rates. Thus, higher pressure loss was induced and consequently higher CP power was demanded, according to Eq. 24 and 27. Furthermore, it was found by simulations that if fixing the flow velocities by scaling the flow rates proportionally to the width, a constant SEEC of DCMD-based module can also be attained. Conclusively, the surface dimensions (width *W* and length *L*) do not influence sensibly the production and specific consumption, thus the scale-up of the module can be achieved simply by bigger module surface or several modules in parallel.

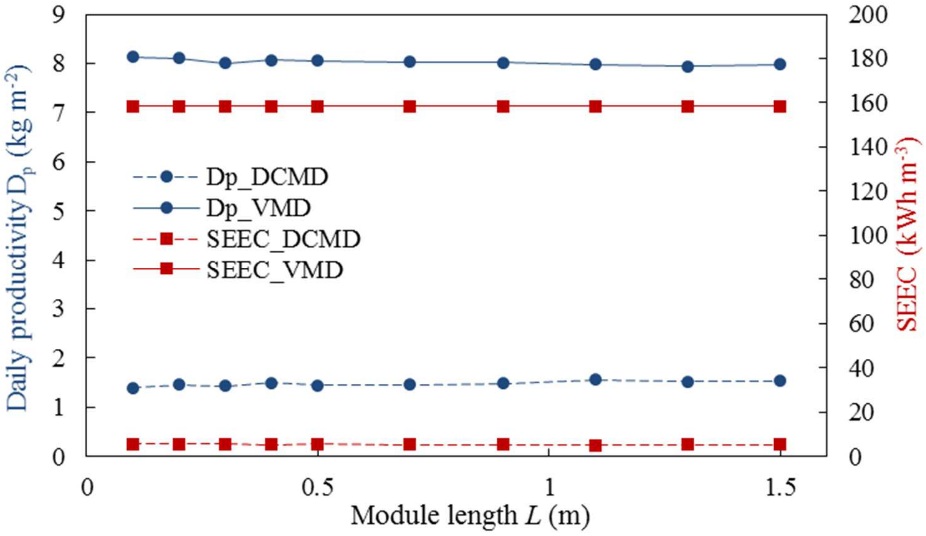

Daily productivity D$_p$ (kg m^{-2})
SEEC (kWh m^{-3})
Module length L (m)
Dp_DCMD
Dp_VMD
SEEC_DCMD
SEEC_VMD

(a)

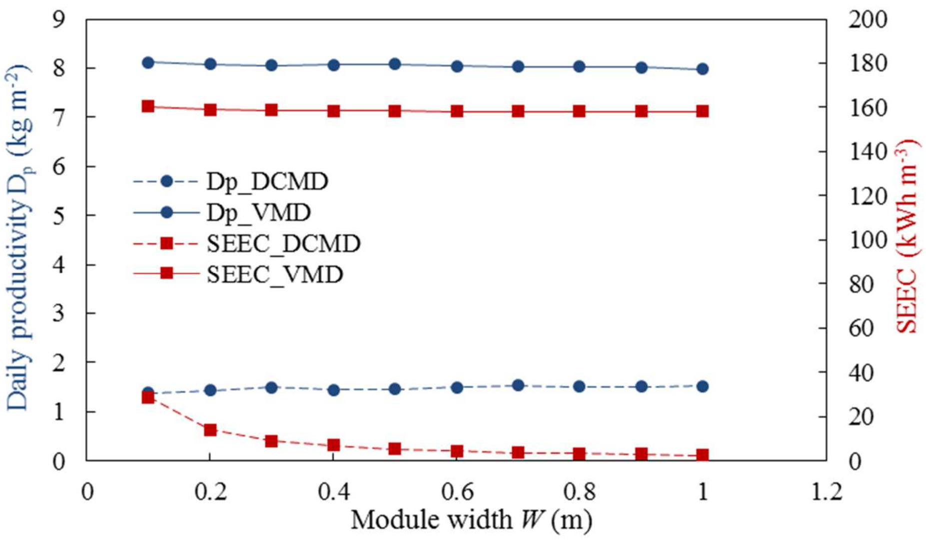

Daily productivity D$_p$ (kg m^{-2})
SEEC (kWh m^{-3})
Module width W (m)
Dp_DCMD
Dp_VMD
SEEC_DCMD
SEEC_VMD

(b)

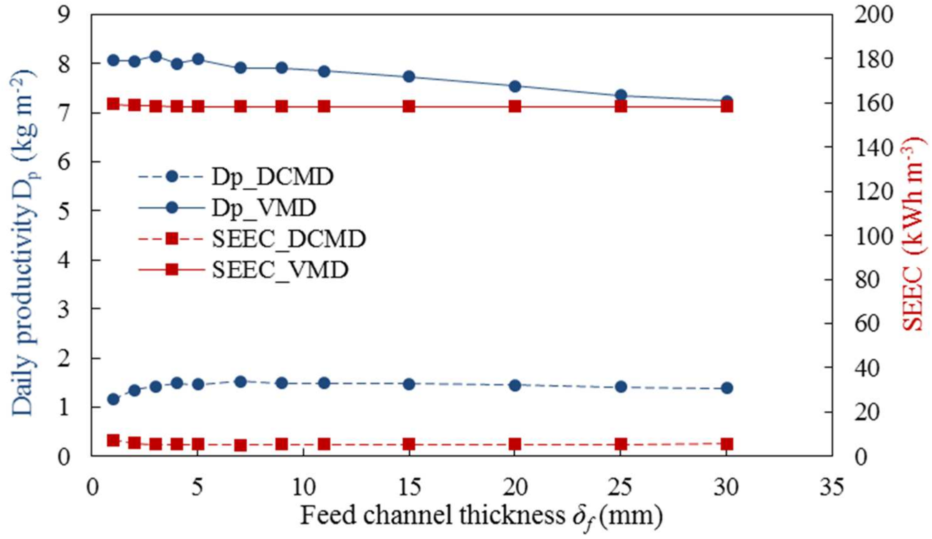

(c)

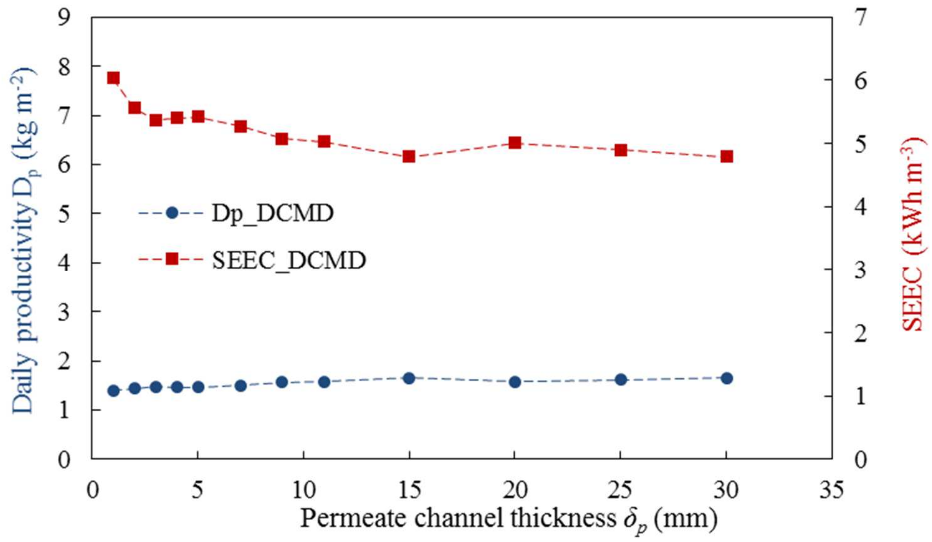

(d)

Figure 12: Daily distillate productivity and specific electrical energy consumption at varying module dimensions for DCMD-FPC and VMD-FPC systems: (a) length L, (b) width W, (c) thickness of feed channel δ_f ($W \times L$ = 0.5×0.7m^2), (d) thickness of permeate channel δ_p ($W \times L$ = 0.5×0.7m^2)

The thickness of the channels had a smaller impact on the flow Reynolds number based on its slightness compared to the width W. The hydraulic diameter of the flow channel was thus nearly double the value of the thickness ($d_h = 2W\delta/(W+\delta) \approx 2\delta$), combined by the flow velocity which was in inverse proportion with the thickness at given flow rates ($v = F_V/(W\delta)$), the effect of the thickness on Re calculation was therefore almost eliminated. From Figure 12c, different trends of the productivities for the VMD-based and DCMD-based systems emerged. When the feed channel thickness was smaller than 5 mm, the D of the VMD-based system held steady while the D of the DCMD-based system slowly went up. After the value of 5 mm, the former slowly went down while the latter also went down. A thinner layer of feed channel helps to enhance heat convection and alleviate temperature polarization for higher permeate flux [67], that is why the D_p of VMD-based module kept on decreasing with higher δ_f. However, the overall heat input from solar absorption limited the production to a certain level even the feed channel was thinner than 5 mm. On the other hand, a thinner feed channel of DCMD also reinforced the heat transfer and brought the temperatures at the bulk and at the membrane surface closer. However, larger transmembrane temperature difference was created simultaneously, admitting greater conductive heat loss and thus reducing the overall accumulated water production, which was already addressed as the one of the major factors in determining the production capacity of the DCMD-FPC system. After a certain thickness, the heat transfer condition inside the feed channel started to take part in the water production, and a rather slight decrease from 1.53 to 1.39 kg m^{-2} at a feed channel thickness from 7 mm to 30 mm was discovered. Besides, the pressure loss by friction along the flow channel was consequently in inverse proportion with δ^3 according to the first term on the right in Eq. 24. As a result, thinner channels induced higher circulation pump consumption, especially when at extremely small value, as observed in the Figure 12c and 12d, though not really outstanding compared to the huge overall electric consumption of the VMD-based module mostly consumed by vacuum pump. At last, the variation of D_p with varying permeate channel thickness δ_p in Figure 12d might probably be explained also by the more important heat loss with thinner flow channels, as explained for δ_f of the feed channel.

3.4. Discussions on potential: Heat recovery & solar concentration

Both solar-integrated MD systems studied in this work have relatively low water productions due to the enormous heat consumption by feed evaporation and the limited thermal energy source provided only by direct solar absorption. This highlights clearly the importance of enhancing the thermal energy income for the feed circulation in case an increase in permeate flux and water production is desired. Generally, two approaches can be conceived in the current application:

Heat recovery from the permeate side back to the feed circulation, and solar concentration to multiply the absorbed heat by the module.

In addition, the daily operations in wintertime (February 1st) are evaluated in this section as well, in parallel with the operations in summertime. Besides the recalculation of solar radiation in winter, certain environmental parameters also have to be altered. Source seawater temperature is set to 13°C on Feb 1st, according to the data for seawater temperature in Barcelona [68], which is not far from Toulouse. Correction factors (r_0, r_1, r_k) for mid-latitude places are configured to 1.03, 1.01 and 1.00 for winter, instead of the values in Table 1 for summer. Finally, an ambient temperature ranging from 0°C to 10°C in winter is considered.

3.4.1 Heat recovery ($A_m = A_c = 0.5 \times 0.7 m^2$)

For the DCMD-FPC module, the heat recovery is usually carried out by recuperating the thermal energy from the cold distillate or the cooling water. In our design, the cooling was carried out by direct heat exchanging between the distillate and the circulating seawater. Therefore, a fixed heat recovery ratio (HRR) of all the heat exchanged by cooling was deemed as a relevant way to study the influence of heat recovery on system performance. On the other hand, for the VMD-FPC module, a certain ratio of the permeate vapor was presumed to be condensed by a certain facility before the vacuum pump, whose heat was redirected to the feed circulation. Thus, this ratio in VMD equals to a fixed HRR of all the condensation heat of the permeate. However, the discussion was incapable of evaluating the corresponding amount of supplementary electricity demand for both heat recovery approaches.

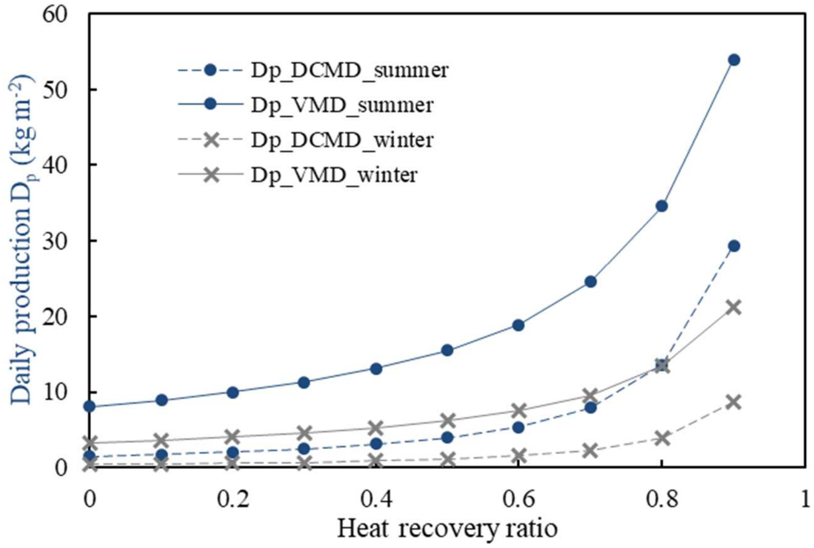

Figure 13: Daily distillate production D_p for DCMD-FPC and VMD-FPC systems at varying heat recovery ratios (HRR) in both summer and winter

Figure 13 demonstrates a substantial increase in water productivity for both systems if heat recovery strategies are implemented. In summer, the D_p of the DCMD system was markedly improved from around 1.5 kg m^{-2} without heat recovery to nearly 30 kg m^{-2} with 0.9 of the heat gained by the cooling stream being put back to the feed. Regarding the VMD system, the increment of D_p was from around 8 kg m^{-2} to even more than 50 kg m^{-2}. Compared with operating in summer, D_p of DCMD-FPC in winter drastically decreased by more than 70%, while D_p of VMD-FPC in winter was lowered by around 60%. In an HRR range of 0 ~ 0.8, the production of VMD-FPC in winter is even higher than that of DCMD-FPC in summer, revealing the huge advantage of the former over the latter in terms of freshwater provision capacity.

However in reality, a high HRR is not easy to attain. For DCMD, the vapor condensation directly takes place inside the cold distillate, whose temperature has to be low enough to maintain the driving force for vapor transfer, thus the latent heat of the permeate vapor is then stored in the cold distillate in liquid phase. Therefore, this heat is hard to be directly recovered back to a liquid feed at higher temperature. For VMD, the temperature of the permeate side is even lower in the vacuum, thus the same difficulty exists for heat recovery. However, the latent heat is still stored in vapor phase on the permeate side, which might be recaptured through the condensation elsewhere. Considering such difficulty in heat recovery, high HRRs are not quite realistic and feasible, especially for the DCMD-FPC system. If applying an intermediate HRR (0.3 to 0.7) to a small module of 1 m^2, the potential production of the DCMD-FPC system would still be much too low (2.5 to 7.9 kg in summer; 0.7 to 2.3 kg in winter) compared with the VMD-FPC system (11.3 to 24.6 kg in summer; 4.6 to 9.6 kg in winter). Even on Aug 1st, when the solar condition might be the best on the northern hemisphere, the production of DCMD-FPC can hardly fulfill the drinking demand (2 L per day per person [69]) of a small family. Added by the above discussion on the heat recovery possibilities on both systems, VMD-FPC is therefore reckoned to be the one that is worth further study towards application. It is however needed to check the existence and the feasibility of an innovative approach for heat recovery in the VMD-FPC system and further to evaluate its relevance in terms of extra energy requirements.

3.4.2. Solar concentration ($A_m = A_c = 0.5\times0.7 m^2$)

A solar concentration ratio (CR) is defined as the solar aperture area to absorber area, which can be approximated by the factor of the increment of the absorbed solar energy on the absorber-plate [70]. Only low concentration ratio (e.g. CPC, V-trough) has been applied to MD applications in the literature [71–73]. Indeed, it was found here that a concentration ratio over 7 could lead to a feed temperature over 100°C in the afternoon for both DCMD and VMD-based systems, which was then rejected by the simulation. Consequently, Figure 14 illustrated the water productions of DCMD-FPC and VMD-FPC with varying concentration ratios up to 7, in both summer and winter. Similar to the discussion on the heat recovery, the extra energy consumption by solar tracking systems for the concentrator and other supplementary facilities could not be evaluated at current stage.

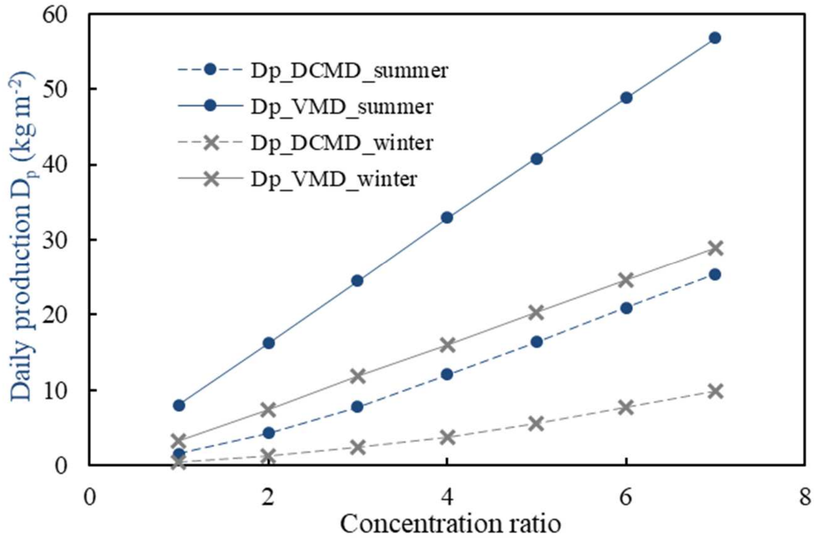

Figure 14: Daily distillate productivity D_p for DCMD-FPC and VMD-FPC systems at varying concentration ratios (CR) in both summer and winter

Unlike Figure 13, the production linearly responded to the increasing CR due to the linear increments in the heat supply by the absorbed solar energy. The production capacity difference between DCMD and VMD-based systems is still obvious, and D_p of VMD-FPC in winter is always even higher than that of DCMD-FPC in summer, similar to the discussion on HRR. At a moderate CR of 3, the D_p of VMD-FPC could reach up to 24.5 kg m^{-2} in summer and 11.8 kg m^{-2} in winter, while that of DCMD-FPC was only able to yield a production of 7.8 kg m^{-2} in summer and 2.4 kg m^{-2} in winter, even lower than the VMD-FPC without heat recovery or solar concentration. D_p of DCMD-FPC also became interesting only when CR was over 6, in terms of the domestic drinking water provision (> 8 kg m^{-2} in winter). However, larger CR would leave larger footprint, decreasing the compactness and the mobility of the system. For example, CR = 6 means a concentrator of an aperture area of more than 6 m^2 needs to be installed for a module of 1 m^2. Furthermore, the complexity in concentrator design and solar-tracking when increasing CR adds to the problem of applicability in remote communities. At last, the design of solar concentrator is also part of the module design, which demands further study.

4. Conclusions

Based on a previous design of an integrated module coupling direct solar heating with VMD process (VMD-FPC system), a similar DCMD-based desalination system was studied in order to contrast the two diametrically opposite MD technologies in terms of water production and power consumption and to compare their hybridization potentials when coupled with direct solar heating scenarios. To provide a fair comparison between the original VMD-FPC module and the DMCD-FPC, a similar dynamic recycling system was indeed defined. Simulations for daily 12-hour operations revealed that the water production of the DCMD-FPC system (0.51L for the 0.35 m^2 module) was much lower than that of the VMD-FPC system (2.83L for the same 0.35 m^2 module) under the same parameters and operating conditions, which indicated a huge difference in the thermal efficiency of utilizing solar energy for distillate production: 16% of the former system and 89% of the latter system. However, much higher production and thermal efficiency also came with a price: electric consumption of VMD-FPC was 0.45 kWh (power consumption per unit distillate 13.25 W L^{-1}), in contrast with only 2.76×10^{-3} kWh of DCMD-FPC (power consumption per unit distillate 0.45 W L^{-1}). Nevertheless, the calculated SCOW of VMD-FPC was still much cheaper than that of DCMD-FPC.

Roles of different groups of parameters concerning material properties, operating conditions, position and dimensions were analyzed in details for both the DCMD-FPC and the VMD-FPC systems, comparatively. The discussions on the variations of the parameters all indicated that in the case of direct solar heating with the limited available solar energy, especially when no heat recovery strategy is applied, the VMD-FPC system was restrained by the heat income from solar energy, while the DCMD-system was even further suppressed by the heat conduction from the feed to the distillate. Besides, the performances of both systems stayed unaffected by the variation of the module surface, which enables a flexible design of the module size based on the productivity and the water provision demand.

Finally, heat recovery and solar concentration were deemed as two possible approaches to enhance the freshwater production of such hybridization. Regarding the former, heat has to be redirected from the low-temperature permeate side to the high-temperature feed circulation in both DCMD and VMD, while the vapor-phase permeate side in VMD enables more possibilities.

Furthermore, the production capacity of a small-scale DCMD-FPC system was shown to be incapable of supplying the drinking water demand for dispersed communities under a reasonable heat recovery ratio, while the VMD-FPC system exhibited a more relevant and controllable production. For the latter approach of solar concentration, productivities for both systems could be linearly improved with an increasing solar concentration ratio, displaying good potentials for application. However, 2 ~ 3 times the concentration ratio of the VMD-FPC was required by the DCMD-FPC to produce the same quantity of distillate, which means a much larger footprint and a higher module complexity of the DCMD-FPC module.

Acknowledgment

This work was supported by the ANR (Agence Nationale de la Recherche) project, 2018: LabCom - Membranes pour le traitement d'eaux des Océans avec énergie Solaire en régions Tropicales (MOST); the Fellowship of China Postdoctoral Science Foundation (No.: 2020TQ0186).

Declarations of interest: None.

References

[1] V.G. Gude, Desalination and water reuse to address global water scarcity, Rev Environ Sci Biotechnol. 16 (2017) 591–609. https://doi.org/10.1007/s11157-017-9449-7.

[2] P. Jacob, S. Laborie, C. Cabassud, Visualizing and evaluating wetting in membrane distillation: New methodology and indicators based on Detection of Dissolved Tracer Intrusion (DDTI), Desalination. 443 (2018) 307–322. https://doi.org/10.1016/j.desal.2018.06.006.

[3] E. Drioli, A. Ali, F. Macedonio, Membrane distillation: Recent developments and perspectives, Desalination. 356 (2015) 56–84. https://doi.org/10.1016/j.desal.2014.10.028.

[4] K.W. Lawson, D.R. Lloyd, Membrane distillation, Journal of Membrane Science. 124 (1997) 1–25. https://doi.org/10.1016/S0376-7388(96)00236-0.

[5] J.-P. Mericq, S. Laborie, C. Cabassud, Vacuum membrane distillation for an integrated seawater desalination process, Desalination and Water Treatment. 9 (2009) 287–296. https://doi.org/10.5004/dwt.2009.862.

[6] Q. Ma, A. Ahmadi, C. Cabassud, Direct integration of a vacuum membrane distillation module within a solar collector for small-scale units adapted to seawater desalination in remote places: Design, modeling & evaluation of a flat-plate equipment, Journal of Membrane Science. 564 (2018) 617–633. https://doi.org/10.1016/j.memsci.2018.07.067.

[7] D. González, J. Amigo, F. Suárez, Membrane distillation: Perspectives for sustainable and improved desalination, Renewable and Sustainable Energy Reviews. 80 (2017) 238–259. https://doi.org/10.1016/j.rser.2017.05.078.

[8] N. Thomas, M.O. Mavukkandy, S. Loutatidou, H.A. Arafat, Membrane distillation research & implementation: Lessons from the past five decades, Separation and Purification Technology. 189 (2017) 108–127. https://doi.org/10.1016/j.seppur.2017.07.069.
[9] A. Deshmukh, C. Boo, V. Karanikola, S. Lin, A.P. Straub, T. Tong, D.M. Warsinger, M. Elimelech, Membrane Distillation at the Water-Energy Nexus: Limits, Opportunities, and Challenges, Energy Environ. Sci. (2018). https://doi.org/10.1039/C8EE00291F.
[10] R. Miladi, N. Frikha, S. Gabsi, Exergy analysis of a solar-powered vacuum membrane distillation unit using two models, Energy. 120 (2017) 872–883. https://doi.org/10.1016/j.energy.2016.11.133.
[11] P.A. Hogan, Sudjito, A.G. Fane, G.L. Morrison, Desalination by solar heated membrane distillation, Desalination. 81 (1991) 81–90. https://doi.org/10.1016/0011-9164(91)85047-X.
[12] Z. Ding, L. Liu, M.S. El-Bourawi, R. Ma, Analysis of a solar-powered membrane distillation system, Desalination. 172 (2005) 27–40. https://doi.org/10.1016/j.desal.2004.06.195.
[13] S.T. Bouguecha, S.E. Aly, M.H. Al-Beirutty, M.M. Hamdi, A. Boubakri, Solar driven DCMD: Performance evaluation and thermal energy efficiency, Chemical Engineering Research and Design. 100 (2015) 331–340. https://doi.org/10.1016/j.cherd.2015.05.044.
[14] H.C. Duong, L. Xia, Z. Ma, P. Cooper, W. Ela, L.D. Nghiem, Assessing the performance of solar thermal driven membrane distillation for seawater desalination by computer simulation, Journal of Membrane Science. 542 (2017) 133–142. https://doi.org/10.1016/j.memsci.2017.08.007.
[15] A.E. Kabeel, M. Abdelgaied, E.M.S. El-Said, Study of a solar-driven membrane distillation system: Evaporative cooling effect on performance enhancement, Renewable Energy. 106 (2017) 192–200. https://doi.org/10.1016/j.renene.2017.01.030.
[16] X. Wang, L. Zhang, H. Yang, H. Chen, Feasibility research of potable water production via solar-heated hollow fiber membrane distillation system, Desalination. 247 (2009) 403–411. https://doi.org/10.1016/j.desal.2008.10.008.
[17] Y. Wang, Z. Xu, N. Lior, H. Zeng, An experimental study of solar thermal vacuum membrane distillation desalination, Desalination and Water Treatment. 53 (2015) 887–897. https://doi.org/10.1080/19443994.2014.927187.
[18] H. Deng, X. Yang, R. Tian, J. Hu, B. Zhang, F. Cui, G. Guo, Modeling and optimization of solar thermal-photovoltaic vacuum membrane distillation system by response surface methodology, Solar Energy. 195 (2020) 230–238. https://doi.org/10.1016/j.solener.2019.11.006.
[19] Q. Ma, Z. Xu, R. Wang, Distributed solar desalination by membrane distillation: current status and future perspectives, Water Research. 198 (2021) 117154. https://doi.org/10.1016/j.watres.2021.117154.
[20] K. Murase, Y. Yamagishi, K. Tano, Development of a hybrid solar distillator of a basin type distillator and a membrane distillator, Desalination and Water Treatment. 9 (2009) 96–104. https://doi.org/10.5004/dwt.2009.757.
[21] T.-C. Chen, C.-D. Ho, Immediate assisted solar direct contact membrane distillation in saline water desalination, Journal of Membrane Science. 358 (2010) 122–130. https://doi.org/10.1016/j.memsci.2010.04.037.
[22] J.-P. Mericq, S. Laborie, C. Cabassud, Evaluation of systems coupling vacuum membrane distillation and solar energy for seawater desalination, Chemical Engineering Journal. 166 (2011) 596–606. https://doi.org/10.1016/j.cej.2010.11.030.

[23] S.B. Abdallah, N. Frikha, S. Gabsi, Study of the performances of different configurations of seawater desalination with a solar membrane distillation, Desalination and Water Treatment. 52 (2014) 2362–2371. https://doi.org/10.1080/19443994.2013.792746.
[24] Q. Li, L.-J. Beier, J. Tan, C. Brown, B. Lian, W. Zhong, Y. Wang, C. Ji, P. Dai, T. Li, P. Le Clech, H. Tyagi, X. Liu, G. Leslie, R.A. Taylor, An integrated, solar-driven membrane distillation system for water purification and energy generation, Applied Energy. 237 (2019) 534–548. https://doi.org/10.1016/j.apenergy.2018.12.069.
[25] A. Bamasag, T. Alqahtani, S. Sinha, N. Ghaffour, P. Phelan, Solar-heated submerged vacuum membrane distillation system with agitation techniques for desalination, Separation and Purification Technology. 256 (2021) 117855. https://doi.org/10.1016/j.seppur.2020.117855.
[26] A. Bamasag, T. Alqahtani, S. Sinha, N. Ghaffour, P. Phelan, Experimental investigation of a solar-heated direct contact membrane distillation system using evacuated tube collectors, Desalination. 487 (2020) 114497. https://doi.org/10.1016/j.desal.2020.114497.
[27] A. Criscuoli, M.C. Carnevale, E. Drioli, Evaluation of energy requirements in membrane distillation, Chemical Engineering and Processing: Process Intensification. 47 (2008) 1098–1105. https://doi.org/10.1016/j.cep.2007.03.006.
[28] C. Huayan, W. Chunrui, J. Yue, W. Xuan, L. Xiaolong, Comparison of three membrane distillation confi gurations and seawater desalination by vacuum membrane distillation, Desalination and Water Treatment. 28 (2011) 321–327. https://doi.org/10.5004/dwt.2011.1605.
[29] H. Fan, Y. Peng, Application of PVDF membranes in desalination and comparison of the VMD and DCMD processes, Chemical Engineering Science. 79 (2012) 94–102. https://doi.org/10.1016/j.ces.2012.05.052.
[30] J. Koo, J. Han, J. Sohn, S. Lee, T.-M. Hwang, Experimental comparison of direct contact membrane distillation (DCMD) with vacuum membrane distillation (VMD), Desalination and Water Treatment. 51 (2013) 6299–6309. https://doi.org/10.1080/19443994.2013.780817.
[31] G. Guan, X. Yang, R. Wang, R. Field, A.G. Fane, Evaluation of hollow fiber-based direct contact and vacuum membrane distillation systems using aspen process simulation, Journal of Membrane Science. 464 (2014) 127–139. https://doi.org/10.1016/j.memsci.2014.03.054.
[32] L. Eykens, T. Reyns, K. De Sitter, C. Dotremont, L. Pinoy, B. Van der Bruggen, How to select a membrane distillation configuration? Process conditions and membrane influence unraveled, Desalination. 399 (2016) 105–115. https://doi.org/10.1016/j.desal.2016.08.019.
[33] V. Karanikola, S.E. Moore, A. Deshmukh, R.G. Arnold, M. Elimelech, A.E. Sáez, Economic performance of membrane distillation configurations in optimal solar thermal desalination systems, Desalination. 472 (2019) 114164. https://doi.org/10.1016/j.desal.2019.114164.
[34] S. Kim, S. Kim, Z. Ahmed, D.K. Cha, J. Cho, Flux model for the membrane distillation process to treat wastewater: effect of solids concentration, Journal of Membrane Science. (2018). https://doi.org/10.1016/j.memsci.2018.09.018.
[35] J. Zhang, J.-D. Li, M. Duke, M. Hoang, Z. Xie, A. Groth, C. Tun, S. Gray, Modelling of vacuum membrane distillation, Journal of Membrane Science. 434 (2013) 1–9. https://doi.org/10.1016/j.memsci.2013.01.048.
[36] J. Phattaranawik, R. Jiraratananon, A.G. Fane, Heat transport and membrane distillation coefficients in direct contact membrane distillation, Journal of Membrane Science. 212 (2003) 177–193. https://doi.org/10.1016/S0376-7388(02)00498-2.

[37] A. Bahmanyar, M. Asghari, N. Khoobi, Numerical simulation and theoretical study on simultaneously effects of operating parameters in direct contact membrane distillation, Chemical Engineering and Processing: Process Intensification. 61 (2012) 42–50. https://doi.org/10.1016/j.cep.2012.06.012.
[38] I. Hitsov, T. Maere, K. De Sitter, C. Dotremont, I. Nopens, Modelling approaches in membrane distillation: A critical review, Separation and Purification Technology. 142 (2015) 48–64. https://doi.org/10.1016/j.seppur.2014.12.026.
[39] M. Rabie, M.F. Elkady, A.H. El-Shazly, Effect of channel height on the overall performance of direct contact membrane distillation, Applied Thermal Engineering. 196 (2021) 117262. https://doi.org/10.1016/j.applthermaleng.2021.117262.
[40] J.-P. Mericq, Approche intégrée du dessalement d'eau de mer: Distillation membranaire sous vide pour la réduction des rejets salins et possibilités de couplage avec l'énergie solaire, 2009. http://eprint.insa-toulouse.fr/archive/00000341/ (accessed February 12, 2016).
[41] R.W. Schofield, A.G. Fane, C.J.D. Fell, Heat and mass transfer in membrane distillation, Journal of Membrane Science. 33 (1987) 299–313. https://doi.org/10.1016/S0376-7388(00)80287-2.
[42] R. Long, X. Lai, Z. Liu, W. Liu, Direct contact membrane distillation system for waste heat recovery: Modelling and multi-objective optimization, Energy. 148 (2018) 1060–1068. https://doi.org/10.1016/j.energy.2018.02.027.
[43] A. Alkhudhiri, N. Darwish, N. Hilal, Membrane distillation: A comprehensive review, Desalination. 287 (2012) 2–18. https://doi.org/10.1016/j.desal.2011.08.027.
[44] T.L. Bergman, F.P. Incropera, Fundamentals of heat and mass transfer, John Wiley & Sons, 2011.
[45] M.A.E.-R. Abu-Zeid, Y. Zhang, H. Dong, L. Zhang, H.-L. Chen, L. Hou, A comprehensive review of vacuum membrane distillation technique, Desalination. 356 (2015) 1–14. https://doi.org/10.1016/j.desal.2014.10.033.
[46] E.A. Bruges, B. Latto, A.K. Ray, New correlations and tables of the coefficient of viscosity of water and steam up to 1000 bar and 1000°C, International Journal of Heat and Mass Transfer. 9 (1966) 465–480. https://doi.org/10.1016/0017-9310(66)90102-5.
[47] Heat exchanger sizing and rating (ht.hx) — Heat Transfer 0.1 documentation, (n.d.). https://ht.readthedocs.io/en/latest/ht.hx.html (accessed October 19, 2018).
[48] R.K. Shah, A.L. London, Laminar flow forced convection in ducts: a source book for compact heat exchanger analytical data, Academic press, 2014.
[49] V. Gnielinski, New equations for heat and mass-transfer in turbulent pipe and channel flow, International Chemical Engineering. 16 (1976) 359–368.
[50] W.L. McCabe, J.C. Smith, P. Harriott, Unit operations of chemical engineering, McGraw-Hill New York, 1993.
[51] scipy.integrate.ode — SciPy v0.18.1 Reference Guide, (n.d.). https://docs.scipy.org/doc/scipy-0.18.1/reference/generated/scipy.integrate.ode.html (accessed December 14, 2017).
[52] scipy.optimize.fsolve — SciPy v0.14.0 Reference Guide, (n.d.). https://docs.scipy.org/doc/scipy-0.14.0/reference/generated/scipy.optimize.fsolve.html (accessed October 19, 2018).
[53] P. Jacob, Detection and Understanding of Wetting Mechanisms in Vacuum Membrane Distillation Applied to Desalination of Seawater, 2018.

[54] Heat Exchanger Heat Transfer Coefficients, (n.d.). https://www.engineeringtoolbox.com/heat-transfer-coefficients-exchangers-d_450.html (accessed February 8, 2019).
[55] P. Datt, Latent Heat of Vaporization/Condensation, in: V.P. Singh, P. Singh, U.K. Haritashya (Eds.), Encyclopedia of Snow, Ice and Glaciers, Springer Netherlands, Dordrecht, 2011: pp. 703–703. https://doi.org/10.1007/978-90-481-2642-2_327.
[56] M. Papapetrou, A. Cipollina, U. La Commare, G. Micale, G. Zaragoza, G. Kosmadakis, Assessment of methodologies and data used to calculate desalination costs, Desalination. 419 (2017) 8–19. https://doi.org/10.1016/j.desal.2017.05.038.
[57] Q. Ma, Z. Xu, R. Wang, P. Poredoš, Distributed vacuum membrane distillation driven by direct-solar heating at ultra-low temperature, Energy. 239 (2022) 121891. https://doi.org/10.1016/j.energy.2021.121891.
[58] B. CATTANEO, Photovoltaic Geographical Information System (PVGIS), EU Science Hub - European Commission. (2018). https://ec.europa.eu/jrc/en/pvgis (accessed January 16, 2022).
[59] A.N. Mabrouk, H.E.S. Fath, Technoeconomic study of a novel integrated thermal MSF–MED desalination technology, Desalination. 371 (2015) 115–125. https://doi.org/10.1016/j.desal.2015.05.025.
[60] F.E. Ahmed, R. Hashaikeh, N. Hilal, Solar powered desalination – Technology, energy and future outlook, Desalination. 453 (2019) 54–76. https://doi.org/10.1016/j.desal.2018.12.002.
[61] R.G. Raluy, R. Schwantes, V.J. Subiela, B. Peñate, G. Melián, J.R. Betancort, Operational experience of a solar membrane distillation demonstration plant in Pozo Izquierdo-Gran Canaria Island (Spain), Desalination. 290 (2012) 1–13. https://doi.org/10.1016/j.desal.2012.01.003.
[62] D. Winter, Membrane Distillation—A Thermodynamic, Technological and Economic Analysis, University of Kaiserslautern, 2015. https://www.reiner-lemoinestiftung.de/pdf/dissertationen/Dissertation-Daniel_Winter.pdf.
[63] R. Schwantes, K. Chavan, D. Winter, C. Felsmann, J. Pfafferott, Techno-economic comparison of membrane distillation and MVC in a zero liquid discharge application, Desalination. 428 (2018) 50–68. https://doi.org/10.1016/j.desal.2017.11.026.
[64] B. Rahimi, J. May, A. Christ, K. Regenauer-Lieb, H.T. Chua, Thermo-economic analysis of two novel low grade sensible heat driven desalination processes, Desalination. 365 (2015) 316–328. https://doi.org/10.1016/j.desal.2015.03.008.
[65] Database - Energy - Eurostat, (n.d.). https://ec.europa.eu/eurostat/web/energy/data/database (accessed January 17, 2022).
[66] P. Wang, T.-S. Chung, Recent advances in membrane distillation processes: Membrane development, configuration design and application exploring, Journal of Membrane Science. 474 (2015) 39–56. https://doi.org/10.1016/j.memsci.2014.09.016.
[67] J.-G. Lee, S. Jeong, A.S. Alsaadi, N. Ghaffour, Influence of high range of mass transfer coefficient and convection heat transfer on direct contact membrane distillation performance, Desalination. 426 (2018) 127–134. https://doi.org/10.1016/j.desal.2017.10.034.
[68] Mediterranean | Sea Temperatures, (n.d.). http://www.seatemperature.org/mediterranean-sea (accessed February 15, 2019).
[69] How Much Water Should You Drink Per Day?, Healthline. (2018). https://www.healthline.com/nutrition/how-much-water-should-you-drink-per-day (accessed January 10, 2019).

[70] J.A. Duffie, W.A. Beckman, Solar engineering of thermal processes, Wiley New York, 2013.
[71] E. Guillén-Burrieza, J. Blanco, G. Zaragoza, D.-C. Alarcón, P. Palenzuela, M. Ibarra, W. Gernjak, Experimental analysis of an air gap membrane distillation solar desalination pilot system, Journal of Membrane Science. 379 (2011) 386–396. https://doi.org/10.1016/j.memsci.2011.06.009.
[72] E. Guillén-Burrieza, D.-C. Alarcón-Padilla, P. Palenzuela, G. Zaragoza, Techno-economic assessment of a pilot-scale plant for solar desalination based on existing plate and frame MD technology, Desalination. 374 (2015) 70–80. https://doi.org/10.1016/j.desal.2015.07.014.
[73] N.A.S. Elminshawy, M.A. Gadalla, M. Bassyouni, K. El-Nahhas, A. Elminshawy, Y. Elhenawy, A novel concentrated photovoltaic-driven membrane distillation hybrid system for the simultaneous production of electricity and potable water, Renewable Energy. 162 (2020) 802–817. https://doi.org/10.1016/j.renene.2020.08.041.